PASJ: Publ. Astron. Soc. Japan , 1–??,
© 2014. Astronomical Society of Japan.

arXiv:1412.6873v2 [astro-ph.SR] 30 Dec 2014

Near Infrared Spectroscopy of M Dwarfs. II. H_2O Molecule as an Abundance Indicator of Oxygen*

Takashi Tsuji
Institute of Astronomy, School of Science, The University of Tokyo, 2-21-1 Osawa, Mitaka-shi, Tokyo, 181-0015
ttsuji@ioa.s.u-tokyo.ac.jp
Tadashi Nakajima
National Astronomical Observatory of Japan, 2-21-1 Osawa, Mitaka-shi, Tokyo, 181-8588
tadashi.nakajima@nao.ac.jp
and
Yoichi Takeda
National Astronomical Observatory of Japan, 2-21-1 Osawa, Mitaka-shi, Tokyo, 181-8588
takeda.yoichi@nao.ac.jp

(Received ; accepted)

Abstract

Based on the near infrared spectra ($R \approx 20000$) of M dwarfs, oxygen abundances are determined from the ro-vibrational lines of H_2O. Although H_2O lines in M dwarfs are badly blended each other and the continuum levels are depressed appreciably by the collective effect of numerous H_2O lines themselves, quantitative analysis of H_2O lines has been carried out by referring to the pseudo-continua consistently defined by the same way on the observed and theoretical spectra. For this purpose, the pseudo-continuum on the theoretical spectrum has been evaluated accurately by the use of the recent high-precision H_2O line-list. Then, we propose a simple and flexible method of analyzing equivalent widths (EWs) of blended features (i.e., not necessarily limited to single lines) by the use of a mini curve-of-growth (CG), which is a small portion of the usual CG around the observed EW. The mini CG is generated by using the theoretical EWs evaluated from the synthetic spectrum by exactly the same way as the EWs are measured from the observed spectrum. The observed EW is converted to the abundance by the use of the mini CG, and the process is repeated for all the observed EWs line-by-line or blend-by-blend.

In cool M dwarfs, almost all the oxygen atoms left after CO formation are in stable H_2O molecules, which suffer little change for the uncertainties due to imperfect modelling of the photospheres. Moreover, the thermal velocity of H_2O is most probably larger than the micro-turbulent velocity because of its lower molecular weight, and the uncertainty of the micro-turbulent velocity will have relatively minor effect on the abundance determination. Then the numerous H_2O lines are excellent abundance indicators of oxygen. The oxygen abundances are determined to be $\log A_{\rm O}$ ($A_{\rm O} = N_{\rm O}/N_{\rm H}$) between -3.5 and -3.0 in 38 M dwarfs, but cannot in four early M dwarfs in which H_2O lines are detected only marginally. The resulting $\log A_{\rm O}/A_{\rm C}$ plotted against $\log A_{\rm C}$ appears to be systematically smaller in the carbon-rich M dwarfs, showing the different formation histories of oxygen and carbon in the chemical evolution of the Galactic disk. Also, $A_{\rm O}/A_{\rm Fe}$ ratios in most M dwarfs are closer to the solar $A_{\rm O}/A_{\rm Fe}$ ratio based on the classical high oxygen abundance rather than on the recently downward revised low value.

Key words: Molecular data – Stars : abundances – Stars : atmospheres – Stars : fundamental parameters – Stars : low mass

1. Introduction

Presence of water in stellar photospheres has been predicted based on the theory of thermochemistry (e.g. Russell 1934), and the observational confirmation has been done on a Mira variable star at the infancy of the infrared spectroscopy (Kuiper 1962). However, detailed observations of water vapor in celestial objects have been hampered by the obscuration of the water vapor in the Earth's atmosphere. For this reason, the most clear demonstration of the water vapor in stellar atmospheres has been done by the balloon-born telescope known as Stratoscope II on several red giant and supergiant stars (Woolf et al. 1964). This pioneering undertaking had been taken over after 30 years by the Infrared Space Observatory ISO (Kessler et al. 1996), which revealed that water exists everywhere in the Universe. Now, water (H_2O) may be assumed to be the third abundant molecule next to H_2 and CO in the Universe.

Meanwhile, important progress on the high resolution infrared spectroscopy has been achieved already in the 1970's, despite the rather noisy infrared detectors at that time. This has been made possible with

* Based on data collected at Subaru Telescope, which is operated by the National Astronomical Observatory of Japan.

the Fourier Transform Spectroscopy (FTS) pioneered by Connes (1970) and further developed at Kitt Peak National Observatory (e.g., Ridgway & Brault 1984). Based on observation of cool M giant Mira variable stars with the FTS of KPNO 4m Telescope, a detailed study on the high resolution H_2O spectra on celestial object outside the solar system has been done by Hinkle & Barnes (1979) for the first time, with the use of the molecular data on H_2O known at that time. Their analysis based on the curve-of-growth method revealed complicated behaviors of H_2O spectra, and showed the presence of a very cool layer different from the pulsating photospheric layer. This first attempt at analyzing the spectra of H_2O in M-type Miras showed that the H_2O spectra contain a wealth of information on the coolest outer atmosphere where stellar photosphere and cool circumstellar layers interact.

Next detailed study on high resolution celestial H_2O spectra has been initiated with the detection of many H_2O lines on sunspot umbral spectra with the FTS of the National Solar Observatory at Kitt Peak (Wallace & Livingston 1992; Wallace et al. 1995), followed by detailed laboratory analyses of hot H_2O spectra (Polyansky et al. 1997; Zobov et al. 2000; Tereszchuk et al. 2002). Then detailed laboratory and theoretical works on hot water have been continued by many groups as reviewed by Bernath (2002). As the fruits, an extended line-list of hot water based on the laboratory analysis has been completed (Zobov et al. 2008). Also, a high-accuracy H_2O line-list comprising over 500 million transitions has been completed based on an *ab initio* approach (Barber et al. 2006), and compiled in large databases such as HITEMP2010 (Rothman et al. 2010). The recent progress achieved in the molecular database constitutes the most important basis for the high resolution molecular spectroscopy of celestial objects.

On the other hand, H_2O molecule has been recognized as an important source of opacity in cool gaseous mixture such as the photospheres of M-type stars (e.g., Tsuji 1966; Auman 1967), and the H_2O opacity has been applied to initial attempts of constructing model photospheres of M dwarfs (e.g., Auman 1969; Tsuji 1969). The observational manifestations of water in M dwarfs have been done from low resolution spectra and progressive importance of H_2O as an infrared opacity source in cooler M dwarfs has been well established (e.g., Berriman & Reid 1987; Tinney et al. 1993; Jones et al. 1994).

The high resolution spectroscopy has been more difficult for such faint objects as M dwarfs until recently. Even with the FTS, M dwarfs were too faint and we know only one pioneering attempt at analyzing the infrared high resolution spectra of M dwarfs by Mould (1978). However, recent progress in infrared spectroscopy with the new infrared detectors finally made it possible to observe infrared spectra of faint objects including M dwarfs at high resolution (e.g., Önehag et al. 2012). We started to explore such a new possibility opened by the progress of infrared spectroscopy with the use of the echelle mode of InfraRed Camera and Spectrograph, IRCS (Kobayashi et al. 2000) at Subaru.

Although the fundamental parameters such as the effective temperatures needed for spectroscopic analysis were poorly known for M dwarfs until recently, recent progress of stellar interferometry has finally resolved this problem and accurate effective temperatures are now known based on the measured angular diameters. We found that the effective temperatures, $T_{\rm eff}$, based on the interferometry (Boyajian et al. 2012 and references cited therein) and supplemented by those based on the infrared flux method for cooler M dwarfs (Tsuji et al. 1996), show a fairly tight correlation with the absolute magnitudes at 3.4 μm, $M_{3.4}$, based on the WISE data (Wright et al. 2010). Then we proposed a simple method to infer $T_{\rm eff}$ from $M_{3.4}$ available to almost all the M dwarfs we have observed (Tsuji & Nakajima 2014; hereafter be referred to as Paper I).

Another problem in the quantitative analysis of the spectra of M dwarfs is that the continuum levels cannot be seen because of the veil opacity due to numerous molecular lines, especially of H_2O. For this difficulty, we showed that the spectroscopic analysis of M dwarfs can be done by referring to the pseudo-continuum levels both on the observed and theoretical spectra. This is possible since the pseudo-continuum level on the theoretical spectrum can be evaluated accurately thanks to the recently developed high precision H_2O line database (Paper I). It can be shown that the quantitative analysis of the spectrum referring to the pseudo-continuum is essentially the same as that referring to the true-continuum.

In this paper, we use the observed data introduced in Paper I (as for detail, see its Table 1) in which we analyzed the CO spectra. In this paper, we focus our attention to the H_2O spectra. We first summarize the basic physical parameters and model photospheres of M dwarfs we study in this paper (section 2). Then, we examine the H_2O spectra in the K band region (section 3). We analyze a portion of the spectral region with the strong H_2O features in the midst of the 1.9 μm band (section 4) and another portion with relatively sparse H_2O blends in the tail of the H_2O 2.7 μm band (section 5). We will show that H_2O is an excellent abundance indicator of oxygen in M dwarfs (subsection 6.1) and oxygen abundances in 38 M dwarfs have been determined (subsection 6.2). We summarize the method of abundance analysis which is essentially very simple (subsection 6.3). We close our discussion with a prospect on the spectroscopy of H_2O in stellar spectra other than M dwarfs (subsection 6.4).

2. Fundamental Parameters and Model Photospheres of M Dwarfs

We summarize the basic parameters of our 42 program stars in Table 1. Following the object names in the first column, the spectral types given in the second column are from Joy & Abt (1974) for 29 M dwarfs (those beginning with dM in Table 1), from SIMBAD for the 12 cases (those beginning with M), and unknown for the remaining one object (GJ 768.1C). The values of $T_{\rm eff}$ and $\log g$ given in the third and fourth columns, respectively, are those used in our analysis of CO in Paper I. In dis-

cussing the values of $T_{\rm eff}$, however, we used the WISE All-Sky Release in Paper I to obtain $M_{3.4}$, the absolute magnitude based on the WISE $W1$ flux, throughout. Later we notice that there is a new version referred to as the AllWISE Catalog. According to the AllWISE Explanatory Supplement[1], the $W1$ and $W2$ photometric sensitivity is better in the AllWISE Catalog than in the WISE All-Sky data we have applied in Paper I. However, it is also noted that the sources brighter than $W1 < 8$ mag may have better photometry in the WISE All-Sky Catalog than in the AllWISE Catalog.

We have examined the AllWISE data and find that the results for some K and M dwarfs we have used as calibrators of $M_{3.4} - \log T_{\rm eff}$ relation in Paper I were changed to unreasonable values that may suffer the saturation effect or even some objects disappeared from the database. As a result, the number of calibration sources using $T_{\rm eff}$ values by interferometry (Boyajian et al. 2012) decreases from 27 to 15 and those using $T_{\rm eff}$ values by the infrared flux method (Tsuji et al. 1996) from 9 to 7. But we add three new M dwarfs for which angular diameters are measured anew (von Braun et al. 2014) and thus the number of calibration stars is 15 + 7 + 3 = 25 as shown in Tables 10 & 11 (Appendix I). These data of Tables 10 & 11 are plotted in Fig. 18 (Appendix I), on which the mean $M_{3.4} - \log T_{\rm eff}$ relation from Fig. 1 in Paper I is reproduced. Despite some changes in the WISE database, the AllWISE data are consistent with the mean $M_{3.4} - \log T_{\rm eff}$ relation based on the WISE All-Sky Catalog. We reanalyze a few objects with $F_{3.4} > 8$ mag in Table 5 of Paper I with the data of the AllWISE, but the resulting $T_{\rm eff}$ values agree within 10 K with the results based on the WISE All-Sky data. Since most of M dwarfs in Table 5 of Paper I are brighter than $F_{3.4} = 8$ mag, we decide to use the results of Table 5 in Paper I to all the objects[2].

We also apply the same model photospheres used in the analysis of CO in Paper I, and these models are given in the fifth column of Table 1. The model photospheres are designated by cloud type/abundance case/$T_{\rm eff}$ /$\log g$ as in our model database referred to as the unified cloudy model (UCM)[3]. The cloud type is defined to characterize the thickness of the dust cloud formed in the photospheres of cool dwarfs. The dust cloud forms at the condensation temperature $T_{\rm cond}$ and dissolves at a critical temperature $T_{\rm cr}$ because dust particles become too large and precipitate. Thus dust cloud exists in the region of $T_{\rm cr} \lesssim T \lesssim T_{\rm cond}$, where $T_{\rm cond}$ is fixed thermochemically. Then, thickness of the cloud depends on $T_{\rm cr}$ which is a free parameter in our UCMs and used to define the cloud type (as for details see Tsuji 2002; 2005). The cloud type includes a limiting case of no dust cloud (referred to as a clear case, C). Generally, dust clouds are formed in the photospheres of cool dwarfs with $T_{\rm eff}$ below about 2600 K, and hence all our present sample are dust-free. Also, *case a* abundance is based on the classical solar abundance with $\log A_{\rm C}$ = -3.40[4] and $\log A_{\rm O}$ = -3.08 (see Table 1 in Tsuji 2002), and *case c* on the downward revised solar C & O abundances of $\log A_{\rm C}$ = -3.61 and $\log A_{\rm O}$ = -3.31 (Allende Prieto et al. 2002). We used the UCM grid in our preliminary analysis, but generated specified model for $T_{\rm eff}$ and $\log g$ of each object in the subsequent analysis. These models are referred to, for example, as Ca3570c489 implying a clear model without dust cloud, with the *case a* abundance, $T_{\rm eff}$ = 3570 K, and $\log g$ = 4.89.

Table 1: Fundamental parameters and model photospheres (p.27).

3. H_2O in the Spectra of M Dwarfs

3.1. *Molecular Data of H_2O*

We first try to identify H_2O transitions by referring to the laboratory data by Zobov et al. (2008), but we soon notice that the BT2-HITEMP2010 database (Barber et al. 2006; Rothman et al. 2010), which we have already examined in Paper I, provides fairly accurate line positions of H_2O lines. It has generally been thought that the *ab initio* approach to the molecular structure and spectroscopic data provides large line-lists but their accuracy especially on the line positions cannot be very high. However, the recently computed line-list by Barber et al. (2006) attained an accuracy to be used for identifications of H_2O lines at last. Since intensity data are also required for abundance analysis, we decide to use the BT2-HITEMP2010 data in the following analysis. The accurate laboratory data should certainly be useful if we are to study radial velocities, for example.

Under the high density of the photospheres of M dwarfs, pressure broadening plays an important role. Usually, collision half-width γ is represented by

$$\gamma = \gamma_0 \frac{p}{p_0} (\frac{T_0}{T})^n, \qquad (1)$$

where γ_0 is the collision half-width measured at a reference temperature T_0 (e.g. 296 K) and gas pressure p_0. As to pressure broadening coefficients for H_2O perturbed by H_2 and He relevant to stellar photospheres, there are some experimental (e.g., Steyert et al. 2004, Faure et al. 2013) and theoretical (e.g., Gamache et al. 1996) works for pure rotational transitions. We have compared the resulting collision half-widths by the H_2 and He broadening with those by the air broadening for the case of CO and found that they are not drastically different in Table 6 of Paper I. The case of H_2O is found to be more or less the same, and we assume a median value of $\gamma_0 = 0.08\,{\rm cm^{-1}\,atm^{-1}}$

[1] http://wise2.ipac.caltech.edu/docs/release/allwise/expsup.

[2] This also applies to the values of $T_{\rm eff}$ of three objects for which angular diameters have been measured (von Braun et al. 2014) after Paper I was completed, for consistency of our analysis with that of Paper I. Also, we wonder why $T_{\rm eff}$ of GJ 876 by the new interferometric measurement deviates so large from the mean $M_{3.4} - \log T_{\rm eff}$ relation, as shown in Fig. 18 (Appendix I; also see Table 14 in Paper I), as the case of GJ 725B (see Fig. 1 in Paper I).

[3] http://www.mtk.ioa.s.u-tokyo.ac.jp/∼ttsuji/export/ucm2.

[4] We use the notation: $A_{\rm El} = N_{\rm El}/N_{\rm H}$, where $N_{\rm El}$ and $N_{\rm H}$ are the number densities of the element El and hydrogen, respectively.

by the air broadening (e.g., Rothman et al. 2010) for all the H_2O lines in M dwarfs.

3.2. H_2O Spectra in the K Band Region

Water molecule is a tri-atomic asymmetric top molecule having three normal vibration modes with $\nu_1 = 3651.7\,\mathrm{cm}^{-1}$, $\nu_2 = 1595.0\,\mathrm{cm}^{-1}$, and $\nu_3 = 3755.8\,\mathrm{cm}^{-1}$ (Herzberg 1945). In the K band region, the H_2O 2.7 μm band is mainly composed of the ν_1 and ν_3 fundamentals and $2\nu_2$ overtone, while the H_2O 1.9 μm band mainly of the combination bands $\nu_2+\nu_3$ and $\nu_1+\nu_2$. The model spectra of H_2O (with resolution of $R \approx 2000$) based on the BT2-HITEMP2010 line-list for four M dwarf model photospheres of $T_{\rm eff}$ = 2800, 3200, 3600, and 4000 K, assuming the solar metallicity (*case a*), are shown in Fig. 1. The 1.9 μm band is still very weak in the model of $T_{\rm eff}$ = 4000 K and strengthens towards cooler models. The 2.7 μm band is already visible weakly in the model of $T_{\rm eff}$ = 4000 K and appears to be very strong in cooler models.

We choose two portions noted as region A (20296–20391 Å) and region B (22515–22935 Å) in Fig. 1 for our analysis of H_2O spectra. At the top of Fig. 1, the atmospheric window (the K band window) in which atmospheric transmission is larger than 50 % under conditions appropriate for Mauna Kea, Hawaii, is indicated based on the data given by Cox (1999). Both the regions A and B are in the atmospheric window. The region A is in the midst of the 1.9 μm band where H_2O lines are strong. We select this particular region because the atmospheric absorption appears to be relatively weak by visual inspection of the observed spectra. The region B is disturbed by both the 1.9 and 2.7 μm bands least, but nevertheless some H_2O features are found in this region in later M dwarfs. Since H_2O lines in the region A are very strong in later M dwarfs and the pseudo-continua are depressed by as much as 15 % from the true continua[5], we think it's useful to analyze the H_2O lines without such heavy blendings for comparison. The H_2O blends are sparsely distributed in the region B and we survey a larger spectral range to measure a modest number of H_2O blends.

By the way, we have confined our analysis of CO lines in Paper I to the bandhead region of the CO 2-0 band, and it is confirmed in Fig. 1 that this region adjacent to the region B is disturbed by both the H_2O 1.9 and 2.7 μm bands least and that it may be more difficult to analyze CO spectra in other regions, because of the severe blending of H_2O lines.

Fig. 1: Model spectra of M dwarfs in the K band region (p.14).

[5] It is of course not possible to see the true-continuum level in the observed spectrum of M dwarf, but it can be estimated with the help of the theoretical spectrum, as will be shown in subsection 4.3.

3.3. H_2O Spectra in the Region A

As examples of the observed spectra in the region A near 2.0 μm, the cases of four M dwarfs are shown in Fig. 2. We select candidates of H_2O blends to be measured for abundance analysis and indicate them by arrows with reference numbers A01–A17. The total number of H_2O lines in the region A (20296–20391 Å) from BT2-HITEMP2010 line-list with the cut off at the integrated intensity $S(T=3000\,\mathrm{K}) \approx 3.10^{-27}\mathrm{cm}^{-1}\,\mathrm{molecule}^{-1}$ is 69909 lines or about 736 lines per 1 Å interval, and we only show the strong line(s) near the position indicated by each arrow in Table 2[6]. Following the reference number and the observed wavelength (in vacuum) in the columns 1 and 2, respectively, the wavelength, assignments of the upper and lower vibrational levels and of the upper and lower rotational levels, $\log gf$ value, and the lower excitation potential (in cm^{-1}) from the BT2-HITEMP2010 are given successively after the column 3. The vibrational level is defined by the three quantum numbers $v_1v_2v_3$ representing the vibrational states of the three fundamental vibrations. The rotational level is defined by the three parameters J, K_a, and K_c: J is the rotational quantum number of the total angular momentum, K_a and K_c are the quasi-quantum numbers that in the limiting cases of the prolate and oblate symmetric rotors would become the the quantum numbers of the angular momenta associated with the respective figure axes (King et al. 1943).

In the early M dwarf GJ 338A shown in Fig. 2a, H_2O lines are still weak as can be inferred from Fig. 1, but almost all the features shown by the arrows are definitely confirmed as due to H_2O lines in this dM0.5 dwarf. However, in other early type M dwarfs, GJ 380 (dM0.5), GJ 820B (dM0), GJ 884 (dM0.5), and HIP 12961 (M0), these H_2O features are not necessarily very clear and cannot definitely be identified, even though some of the H_2O features can be recognized. Except for these four M dwarfs, the features indicated by the arrows are definitely confirmed as due to H_2O lines in 38 M dwarfs out of our 42 M dwarfs. For examples, H_2O features are well developed in the dM2.5 dwarf GJ 15A, shown in Fig. 2b, and increasingly stronger in later M dwarfs as in the dM4 dwarf GJ 611B shown in Fig. 2c. In the coolest M dwarf GJ 406 in our sample, H_2O features are very strong as shown in Fig. 2d. The spectrum of the B type dwarf Regulus (α Leo, B7V) shown in Fig. 2e reveals the telluric lines mostly due to water vapor. Even though the region A is in the midst of the H_2O 1.9 μm band, the telluric H_2O lines are not so strong in this region A within the atmospheric K window, and have been removed in the observed spectra of M dwarfs rather well during the data reduction with Regulus as calibrator.

Finally, we measure the equivalent widths (EWs) of the H_2O blends by referring to the pseudo-continuum of each

[6] It must be noted that this line-list can never be used for the actual analysis of the spectra and for generating the synthetic spectra, since the effect of the underlying and nearby weak H_2O lines are quite appreciable. The full line-list including all the weak lines must be applied even to evaluate the spectrum of a single blend feature.

object. We select those features whose profiles are well defined both on their left and right wings and, as a result, not all the blends marked by arrows in Fig. 2 are measured. The resulting values of $\log(W/\lambda)_{\rm obs}$ (where W is equivalent width) for the H_2O blends with the reference numbers indicated are given in Table 3.

Fig. 2: H_2O in the region A of the observed spectra (p.15).

Table 2: H_2O blends in the region A (p.28).

Table 3: $\log(W/\lambda)_{\rm obs}$ of H_2O blends in the region A (for online version only) (p.29).

3.4. H_2O Spectra in the Region B

As an example of the observed spectrum in the region B near 2.3 μm, the case of the coolest M dwarf in our sample, GJ 406 (dM6.5), is shown in Fig. 3. In this region, we may not expect to find many stellar H_2O lines from Fig. 1. However, we already know that there are many weak H_2O features in the region of CO 2-0 band just adjacent to the region B (Paper I) and we find that there are considerable number of weak features possibly due to H_2O blends in our higher resolution spectra ($R \approx 20000$ compared to $R \approx 2000$ of Fig. 1) of later M dwarfs. We mark these features again by arrows in Fig. 3 with reference numbers B01–B27. The features marked by arrows are in fact mostly identified as due to stellar H_2O lines by referring to the BT2-HITEMP2010 line-list. The transition(s) that give the large contribution(s) to each feature are given in Table 4, in the same format as in Table 2. The total number of H_2O lines in the region B (22515 – 22935 Å) from BT2-HITEMP2010 line-list with the cut-off at $S(T=3000\,{\rm K}) \approx 3.10^{-27}\,{\rm cm^{-1}\,molecule^{-1}}$ is 317621 lines or about 756 lines per 1 Å interval. Thus it is not possible to measure the isolated single line of H_2O even in this region where blendings are expected to be not so heavy compared to the region A[7], and we had to analyze the blended H_2O features throughout this paper.

In the spectrum of the region B shown in Fig. 3, some strong features are known as due to atomic lines of Ca I in the sunspot umbral spectrum (Wallace & Livingston 1992), and these features are also noted on Fig. 3. The spectrum of Regulus is also shown by the solid (green or grey) line in Fig. 3. There are some strong telluric lines in the region B, and they are due to telluric CH_4 and N_2O rather than H_2O (Mohler 1955). The effect of these telluric absorption has again been removed by Regulus as calibrator during the data reduction, and such a removal of telluric absorption has been done fairly well in general possibly because the telluric absorption in this region is not so strong. In fact, the removal of the telluric absorption in the regions with strong telluric absorption (of over 90% absorption) cannot be done well and some residuals remain occasionally, while inspection of the corrected spectra in the regions A and B does not show such residuals.

We also measure the equivalent widths (EWs) of the H_2O blends by referring to the pseudo-continuum of each object. We can measure the weak H_2O blends in the region B in 20 out of 42 M dwarfs in our sample. These M dwarfs are mostly later than dM3.5 except for the dM2.5 dwarfs pair GJ 797B or are M dwarfs with $T_{\rm eff}$ lower than 3500 K. The resulting values of $\log(W/\lambda)_{\rm obs}$ for the H_2O blends with the reference numbers indicated are given in Table 5.

Fig. 3: H_2O in the region B of the observed spectrum of GJ 406 (p.16).

Table 4: H_2O blends in the region B (p.30).

Table 5: $\log(W/\lambda)_{\rm obs}$ of H_2O blends in the region B (for online version only) (p.31).

4. Analysis of H_2O Lines in the Region A

4.1. Mini Curves-of-Growth Analysis of H_2O Blends

Of the four parameters that characterize stellar spectra, the effective temperature and gravity are known (see Table 1 based on Tables 3, 4, & 5 of Paper I), and we assume the micro-turbulent velocity to be $\xi_{\rm micro} = 1\,{\rm km\,sec^{-1}}$ as in Paper I. Then, the only unknown parameter to be determined from the spectra is abundance. Given that the carbon abundances are already known in Paper I (reproduced in Table 6), rough estimation of the oxygen abundances can be possible. For example, we assume a starting oxygen abundance (logarithmic) to be

$$\log A_{\rm O}^0 = \log A_{\rm C} + 0.30, \qquad (2)$$

where $\log A_{\rm C}$ is the logarithmic carbon abundance from Paper I. Note that this relationship is taken from the solar case (Allende Prieto et al. 2002).

Then, we apply a simple method using mini curve-of-growth blend-by-blend: We generate synthetic spectra for $\log A_{\rm O}^0$ and $\log A_{\rm O}^0 + \delta$ with the carbon abundance and the specific model photosphere for each object from Paper I (also noted in Table 1). We generally assume $\delta = \pm 0.1$ at the beginning. For the H_2O blends for which EWs are measured (Table 3), we evaluate EWs, $W(\delta)$ ($\delta = 0, \pm 0.1$), from the three synthetic spectra we have just prepared, by exactly the same way as we measure the EWs from the observed spectrum. Especially, we refer to the pseudo-continua generally defined consistently both on the observed (see Fig. 2) and predicted spectra.

Now, we have a theoretical mini curve-of-growth defined by $\log(W(\delta)/\lambda)$ vs. $\delta = -0.1, 0.0$, and $+0.1$, where the values of $W(\delta)$ are evaluated from the synthetic spectra as noted above. The value of the abundance correction $\Delta\log A_{\rm O}$ to be consistent with the observed value of $\log(W/\lambda)_{\rm obs}$ from Table 3 can be determined by the use of this mini curve-of-growth. This process is repeated blend-by-blend for all the H_2O blends measured. If the

[7] But the line density in the region B is nearly the same or even larger compared to that in the region A. This is because there are many weak lines even in the region where strong H_2O lines are scarce as in the region B.

resulting values of $\Delta\log A_{\rm O}$ for many blends appear to be less than -0.1, for example, we generate a synthetic spectrum for $\delta = -0.2$ and reanalyze the same data by applying mini curves-of-growth defined by $\log(W(\delta)/\lambda)$ vs. $\delta = -0.2, -0.1$, and 0.0[8]. Finally, we derive the mean abundance correction from the values of $\Delta\log A_{\rm O}$ by all the measured blends.

As an example of the above noted procedure, theoretical mini curves-of-growth for seven selected H_2O blends on the spectrum of GJ 229 are shown by the solid lines in Fig. 4: The reference number of each blend (see Table 3) is shown for the corresponding mini CG, on which the filled circle indicates the values of the observed $\log(W/\lambda)_{\rm obs}$ (read on the ordinate of Fig. 4) and the derived abundance correction $\Delta\log A_{\rm O}$ (read on the abscissa). The resulting seven values of $\Delta\log A_{\rm O}$ and their mean value are shown by the filled circles and dashed line, respectively, in Fig. 5d.

Some other examples of the resulting $\Delta\log A_{\rm O}$ values plotted against the observed values of $\log(W/\lambda)_{\rm obs}$ are shown in Fig. 5 for relatively early M dwarfs, in the order of the decreasing effective temperatures. The number of H_2O blends measured is rather small in the early M dwarfs such as GJ 338B (Fig.5a) and GJ 205 (Fig. 5b), and this is because H_2O lines are still weak and difficult to measure (see Fig. 2). For this reason, the scatter of the data is rather large and accuracy of the results cannot be very high. The number of H_2O blends measured increases for M dwarfs with lower $T_{\rm eff}$ values, and H_2O blends of modest strength in these M dwarfs can be measured fairly accurately. Especially, most of the 17 selected blends in Fig. 2 can be used in M dwarfs such as GJ 411 (Fig. 5i) and GJ 436 (Fig. 5j), and reasonably accurate results can be obtained for these cases.

More or less similar results are obtained in later M dwarfs shown in Fig. 6. However, in the coolest end including GJ 777B (Fig. 6h) and GJ 406 (Fig. 6j), the numbers of blends measured decrease. This should be because the blending is so severe that the line profiles of the H_2O blends cannot be defined well and the number of H_2O blends measured has decreased. Nevertheless, it appears that the mini curves-of-growth analysis on the selected blends works reasonably well even for later M dwarfs in which the continua are depressed by as much as 15 % (subsection 4.3). In Figs. 5 & 6, a remarkable feature is that the abundance corrections $\Delta\log A_{\rm O}$ plotted against the observed values of $\log(W/\lambda)_{\rm obs}$ show little systematic effect and distributed nearly horizontally. As a result, the mean abundance correction can be well determined. We will discuss on this result further in subsection 6.1.

The logarithmic abundance correction $\Delta\log A_{\rm O}^{\rm A}$, the resulting logarithmic oxygen abundance

$$\log A_{\rm O}^{\rm A} = \log A_{\rm O}^{0} + \Delta\log A_{\rm O}^{\rm A}, \tag{3}$$

and the number of H_2O blends used for each M dwarf, N_A, are given in the third, fourth, and fifth columns, respectively in Table 6, following the object's name and the logarithmic carbon abundance $\log A_{\rm C}$ from Paper I in the first and second columns, respectively.

[8] We generally do not apply 3-points interpolation formula, but apply linear interpolation averting extrapolation as far as possible.

Fig. 4: Examples of mini curves-of-growth for H_2O blends in GJ 229 (p.17).

Fig. 5: Derived values of the abundance correction $\Delta\log A_{\rm O}^{A}$ from H_2O blends in the region A (early M) (p.18).

Fig. 6: Derived values of the abundance correction $\Delta\log A_{\rm O}^{A}$ from H_2O blends in the region A (late M) (p.18).

Table 6: Mean values of the abundance correction $\Delta\log A_{\rm O}^{A}$ and the resulting $\log A_{\rm O}^{A}$ from H_2O blends in the region A (p.32).

4.2. Synthetic Spectra

We compare the observed spectra with the predicted ones based on the oxygen abundances $\log A_{\rm O}^{\rm A}$ obtained from the H_2O blends in the region A for all the M dwarfs in Table 6, and some results are shown in Fig. 7. In the early M dwarf GJ 338B, the observed H_2O blends (filled circles) are rather weak but most of them can be reproduced well by the predicted spectra (solid line). For this reason, we are sure that we have certainly identified H_2O features in this early M dwarf. In other early M dwarfs including GJ 380, GJ 820B, GJ 884, and HIP 12961, we can recognize a few strong blends as due to H_2O, but other weak features cannot be explained well as due to H_2O lines, and we decide to exclude such cases from our analysis. In other 38 M dwarfs, the observed H_2O blends are reproduced by the predicted spectra fairly well in general, even if the matchings of the observed and predicted spectra are not perfect. Since there may be some unknown blends other than H_2O and some noise due to imperfect cancellations of the atmospheric lines, for example, the perfect matching may anyhow be difficult.

The candidates of H_2O blends used for analysis are reproduced from Fig. 2 and shown by the arrows in Fig. 7c, but not all of these candidates are used in the actual analysis. For example, in the worst case GJ 777B, only five blends ($\log(W/\lambda)_{\rm obs}$ given in Table 3) are used in the analysis as in Fig. 6h. In this case, the pseudo-continuum can be defined (Fig. 7f) but many H_2O features are so strong and blendings are quite severe. For this reason, the profiles cannot reach the pseudo-continuum level and thus are not well defined to meet our criterion to accept the blends for analysis. This result implies that it is difficult to analyze the spectrum composed of the blends of many strong lines even if the pseudo-continuum can be defined. For this reason, we will analyze H_2O blends in the region B where the blendings are not so severe (section 5).

We also evaluate χ^2 values by

$$\chi^2 = \frac{1}{N-1}\sum_{i=1}^{N}\left(\frac{f_{\rm obs}^i - f_{\rm cal}^i}{\sigma_i}\right)^2, \tag{4}$$

where $f_{\rm obs}^i$ and $f_{\rm cal}^i$ are the observed and predicted spectra, both normalized by their pseudo-continua. N is the

number of data points and σ_i is the noise level obtained from the S/N ratio (Table 1 of Paper I) assumed to be independent of i. We evaluate χ^2 values for the predicted spectra based on $\log A_{\rm O}^{\rm A}$ and $\log A_{\rm O}^{\rm A} \pm 0.05$ where $\log A_{\rm O}^{\rm A}$ is the oxygen abundances obtained above (fourth column of Table 6) and 0.05 is about the probable error of the resulting $\log A_{\rm O}^{\rm A}$. The resulting values of χ^2 for $\log A_{\rm O} = \log A_{\rm O}^{A}$ -0.05, +0.0, and +0.05 are shown as χ^2_-, χ^2_0, and χ^2_+ in the sixth, seventh, and eighth columns, respectively, in Table 6. We confirm that the χ^2_0 value for $\log A_{\rm O} = \log A_{\rm O}^{A}$ is smaller than those for $\log A_{\rm O}$ values deviating by about the probable error from $\log A_{\rm O}^{A}$ for each object, except for a few cases. This result implies that our oxygen abundance $\log A_{\rm O}^{\rm A}$ is consistent with the spectral synthesis analysis in most cases.

We now examine the case that the χ^2 value suggests a possible poor fitting. In the worst case GJ 406, χ^2 value is quite large and larger for our resulting oxygen abundance $\log A_{\rm O}^{\rm A}$ than for reduced oxygen abundance (Table 6). We show the observed and predicted spectra for this M dwarf for a) $\log A_{\rm O} = \log A_{\rm O}^{\rm A}$ (χ^2 = 13.204) and b) $\log A_{\rm O} = \log A_{\rm O}^{\rm A}$ - 0.05 (χ^2 = 10.510) in Fig. 8a and 8b, respectively. Also shown are the H_2O blends actually used for the analysis of this M dwarf by the arrows (see Table 3). Inspection of Fig. 8 reveals that the fittings of the H_2O blends used for the analysis (those indicated by the arrows) are in fact better in Fig. 8a with larger χ^2 value than in Fig. 8b with smaller χ^2 value. The reason why χ^2 value is smaller in Fig. 8b should be due to better fittings in the features not used in our analysis. To confirm this, we exclude the spectral region not used for our analysis by masking the region between 20354.5 and 20385.2 Å in our χ^2 analysis (the region filled with yellow or grey in Fig. 8). The result is χ^2 = 11.119 and 11.227 for $\log A_{\rm O}$ = $\log A_{\rm O}^{\rm A}$ and $\log A_{\rm O}^{\rm A}$ -0.05, respectively. Thus, we are now convinced that the result of the mini CG analysis is consistent with the χ^2 analysis.

Fig. 7: Observed and predicted spectra of H_2O in the region A of six M dwarfs (p.19).

Fig. 8: Observed and predicted spectra of H_2O in the region A of GJ 406 (p.20).

4.3. The True- and Pseudo-Continua

The analyses so far are based on the spectra normalized by the pseudo-continua. This is because the true-continuum cannot be seen on the observed spectrum. In the predicted spectrum, the true-continuum is also not shown explicitly, but it can easily be evaluated by considering the continuous opacity alone in computation. The true-continuum levels obtained in this way and the predicted spectra normalized by the true-continua for GJ 338A, GJ 15A, GJ 611B, and GJ 406 are shown in Fig. 9 by the dotted and solid lines, respectively. The pseudo-continuous levels are also shown by the dashed lines on the predicted spectra. The ratios of pseudo- to true-continua, $F_{\rm pc}/F_{\rm tc}$, are estimated to be 0.986, 0.950, 0.841, and 0.856 for the model spectra of GJ 338A, GJ 15A, GJ 611B, and GJ 406, respectively.

Although the true-continuum level cannot be seen in the observed spectrum, it can be estimated from the pseudo-continuum level in the observed spectrum by assuming the same $F_{\rm pc}/F_{\rm tc}$ ratio for the observed spectrum as for the predicted spectrum. This is possible since the pseudo-continua for the observed spectra are defined well as in the predicted spectra in all the M dwarfs of Fig. 9. The observed spectra of GJ 338A, GJ 15A, GJ 611B, and GJ 406 normalized by the true-continua estimated in this way are shown by the filled circles connected by the dotted lines in Fig. 9. From this result, we now know that the pseudo-continua of the observed spectra in GJ 338, GJ 15A, G 611B, and GJ 406 are depressed by 1.4, 5.0, 15.9, and 14.4 %, respectively, from the true-continua.

Fig. 9: True- and pseudo-continua in four representative M dwarfs (p.21).

5. Analysis of H_2O Lines in the Region B

5.1. Mini Curves-of-Growth Analysis of H_2O Blends

In the region B, H_2O lines can be measured in 20 M dwarfs as mentioned in subsection 3.4, and we carry out the mini curve-of-growth analysis blend-by-blend as in subsection 4.1. Some examples of the resulting $\Delta\log A_{\rm O}$ values plotted against the observed values of $\log (W/\lambda)_{\rm obs}$ are shown in Fig. 10 for the same dwarfs in Fig. 6 for comparison. In general, considerable number of blends can be measured in dM3.5 - dM4 dwarfs which are the major constituents of our sample. The number of blends measured is rather small in the dM2.5 dwarf GJ 797B-NE and more difficult in M dwarfs with $T_{\rm eff} \gtrsim 3500$ K. Actually, we measure several possible H_2O blends in the M2 dwarf GJ 250B ($T_{\rm eff}$ = 3567 K), but other predicted H_2O blends cannot be definitively identified and we decide not to include such a case in our analysis. On the other hand, even in M dwarfs with $T_{\rm eff} \lesssim 3500$ K, it is not always possible to find sufficient number of H_2O lines to be analyzed. For example, we cannot obtain oxygen abundances in GJ 411 ($T_{\rm eff}$ = 3465 K) and GJ436 ($T_{\rm eff}$ = 3416 K) from H_2O lines in the region B. We investigate the reason for this and notice that the oxygen abundances in these stars are about $\log A_{\rm O} \approx -3.4$ (Table 6), which are near the lower limit in our M dwarfs (Fig. 17). For this reason, H_2O lines are rather weak in these objects. Thus, the detection of weak H_2O lines depends not only on temperature but also on oxygen abundance.

Even in the cooler dwarfs, the blendings are not so severe and the pseudo-continua are well defined. In fact, the depressions of the continuum levels estimated by the way outlined in subsection 4.3 are 3.7% in the dM2.5 dwarf GJ 797B-NE and 4.8% even for our coolest sample GJ 406. For this reason, measurements of the EWs are easier in the region B than in the region A, and a large number of lines can be measured for such cooler dwarfs including GJ 611B,

GJ 777B, and GJ 406 (Figs. 10h-j). Thus, the region B is definitely better than the region A for the analysis of H_2O abundances in later M dwarfs. Unfortunately, however, the region B is not useful for the early M dwarfs in which H_2O features are very weak.

The value of logarithmic abundance correction $\Delta\log A_{\rm O}^{\rm B}$, the resulting logarithmic oxygen abundance $\log A_{\rm O}^{\rm B}$, and number of H_2O blends in the region B used for the analysis, N_B, are given in the fourth, fifth and sixth columns, respectively, in Table 7, following the object's name, the value of the logarithmic abundance correction $\Delta\log A_{\rm O}^{\rm A}$ and the resulting logarithmic oxygen abundance $\log A_{\rm O}^{\rm A}$ based on the analysis of the region A from Table 6 in the first, second and third columns, respectively.

Fig. 10: Derived values of the abundance correction $\Delta\log A_{\rm O}^{B}$ from H_2O blends in the region B (for the same objects as in Fig. 6) (p.22).

Table 7: Mean values of the abundance correction $\Delta\log A_{\rm O}^{B}$ and the resulting $\log A_{\rm O}^{B}$ from H_2O blends in the region B (p.33).

5.2. *Synthetic Spectra*

Since the H_2O blends are sparsely distributed in the region B, we examine a selected region (about one fourth of the region B) shown in Fig. 11 where relatively large number of H_2O blends are found together. The candidates of the H_2O blends to be analyzed are reproduced from Fig. 3 and shown by the arrows in Fig. 11c, but again not all these candidates are actually analyzed as in the region A. In this region B, the central depths of H_2O features are only about 5 % or so in the earlier sample such as GJ 797B-NE and GJ 687, and never reach 15 % even in the latest M dwarf in our sample GJ 406. The predicted spectra based on the values of $\log A_{\rm O}^{\rm B}$ shown by the solid lines generally reproduce the observed ones shown by the filled circles but some weak features are rather noisy. For such sparsely distributed H_2O blends, χ^2 test may not be useful.

Fig. 11: Observed and predicted spectra of H_2O in the region B of six M dwarfs (p.23).

5.3. *Comparison of the Results from the Regions A and B*

The differences of the values of the logarithmic oxygen abundances $\log A_{\rm O}$ based on the regions A and B are given in the seventh column of Table 7. The differences appear to be less than the probable errors of the analysis in the region A as well as in the region B in most cases. We also plot the values of the logarithmic oxygen abundances $\log A_{\rm O}$ based on the regions B against those based on the region A in Fig. 12 for 20 objects for which analyses are done both in the regions A and B. The results from the regions A and B show no systematic difference and agree well in general.

The result outlined above implies that the analysis of spectra whose continua are depressed by as much as 15 % can provide the results not much different from the spectra whose continua are depressed by less than 5 %. Thus, it is confirmed that the spectral analysis referring to the pseudo-continua works well, and spectra whose continua are depressed by molecular veil opacity can be analyzed only if the pseudo-continua can be predicted accurately by the use of proper molecular data and if the EWs can be measured well by referring to the pseudo-continua.

Fig. 12: Comparison of the logarithmic oxygen abundances from the regions A and B (p.24).

6. Discussion

6.1. *H_2O as an Abundance Indicator of Oxygen*

The major difficulty in stellar abundance analysis is that the derived abundance depends on model photosphere used. For example, the solar carbon and oxygen abundances are revised downward by about 50 % (Allende Prieto et al. 2002) against the classical values (e.g., Anders & Grevesse 1989). This revision is based on a new solar model photosphere referred to as the 3 D model in which a time-dependent dynamical model for the convective zone has been incorporated. It is true that the classical 1 D models are too simple for the real solar photosphere and further sophistication would certainly be welcome. However, verification of the sophisticated models may be by no means easy.

For comparison, we remember another major revision of solar abundance in the past: The downward revision of iron abundance by about 50 %. This revision has been achieved by the use of Fe II lines whose gf-values were measured accurately for the first time instead of the Fe I lines used for a long time (Holweger et al. 1990; Biémont et al. 1991). In solar photosphere, most iron atoms are singly ionized rather than neutral. For this reason, the Fe^+ abundance is relatively insensitive to the change of the physical condition in the line-forming region and hence will not be affected by imperfect modelling of the solar photosphere. Thus, iron abundance could have been determined accurately by the use of the Fe^+ lines for the first time, and the discrepancy between the solar iron abundance and the meteoritic iron abundance (Anders & Grevesse 1989) could have been resolved. This result was further confirmed by Grevesse & Sauval (1999) who succeeded to reconcile abundance results from the FeI and FeII lines with the use of a new solar model photosphere. The abundance determination depends on many factors, of which model photosphere is a crucial one. For this reason, stellar abundance should better be determined from the species that consumes the larger portion of an element and we refer such species as the major species for the element.

In Fig. 13, the abundances of some molecules are plotted

against the depth in four model photospheres of $T_{\rm eff}$ = 2800, 3200, 3600, and 4000 K (the same models as used in Fig. 1). Also, we plot

$$y({\rm CO}) = P_{\rm CO}/(P_{\rm H} + 2P_{\rm H_2}), \quad (5)$$

on logarithmic scale in Fig. 13 by dotted lines. If almost all the carbon atoms are in CO, $\log y({\rm CO}) \approx \log A_{\rm C} \approx -3.4$. This expectation is satisfied in almost all the region of our four models in Fig. 13 and this fact confirms that CO is the major species of carbon in all our cases. Thus the carbon abundance can be determined accurately from CO, the major species of carbon, as noted in Paper I. We also plot

$$y({\rm H_2O}) = P_{\rm H_2O}/(P_{\rm H} + 2P_{\rm H_2}), \quad (6)$$

by dashed lines. If almost all the oxygen atoms left after CO formation are in H_2O, $\log y({\rm H_2O}) \approx \log (A_{\rm O} - A_{\rm C})$. Inspection of Fig. 13 shows that this case is realized for cooler models of $T_{\rm eff}$ = 3200 and 2800 K, and H_2O is the major species of oxygen in these cases. We confirm that the same situation applies to the models of $T_{\rm eff} \lesssim 3400$ K (as for details of the molecular abundances in these models, see the UCM database[3]). In the model of $T_{\rm eff} = 3600$, $P_{\rm H_2O} \approx P_{\rm OH}$ and H_2O is no longer the major species of oxygen in the models of $T_{\rm eff} \gtrsim 3600$ K. Thus, the oxygen abundances determined from H_2O may depend somewhat on models in early M dwarfs of $T_{\rm eff} \gtrsim 3600$ K. Since H_2O lines are anyhow weak in the early M dwarfs, OH may also be used as another abundance indicator of oxygen. Except for the early M dwarfs, H_2O is the major species of oxygen and can be an excellent abundance indicator of oxygen in M dwarfs.

Another advantage of H_2O as abundance indicator may be that its thermal velocity is rather large because of its light weight. In fact, thermal velocity of H_2O at T =3000 K is $\xi_{\rm th} = 1.66\,{\rm km\,sec^{-1}}$. This is considerably larger than the micro-turbulent velocity we have assumed ($\xi_{\rm micro}$ =1 km sec^{-1}). Since actual turbulent velocity in the photospheres of M dwarfs is not likely to be larger than the value we assumed (see e.g., Bean et al. 2006), Doppler broadening of H_2O lines should be dominated by the thermal velocity. This possibility may be consistent with the result that the abundance corrections $\Delta\log A_{\rm O}$ plotted against $\log (W/\lambda)_{\rm obs}$ in Figs. 5, 6, and 10 show little tilt or nearly horizontal as a mean, as noted in subsection 4.1. If Doppler broadening is dominated by the turbulence as in (super)giant stars, the abundance corrections based on the saturated lines depend largely on the assumed turbulent velocity while those based on the weak lines are nearly independent of the assumed velocity, at least for the case of the unblended single lines. In our case of the blended lines in which several hundreds of lines per 1 Å interval are overlapping, it is not known how EWs are influenced by the micro-turbulent velocity, and this problem will be investigated further hopefully with higher resolution spectra.

Since the discovery that the turbulence plays dominant role in the line broadening in stellar spectra (Struve & Elvey 1934), how to determine the turbulent velocity has been one of the major problems in abundance analysis. In fact, one reason why the results of the abundance analyses by different authors do not agree well in general is due to differences of the turbulent velocities applied by different authors. We might have emphasized somewhat too much on the effect of micro-turbulence in the analysis of CO in Paper I even though CO is heavier than H_2O and hence the relative role of the thermal velocity is not so large as in H_2O. Now, so far as the spectral analysis of H_2O in M dwarfs is concerned, the uncertainty due to the micro-turbulent velocity is rather minor because of the larger thermal velocity, and this fact can be regarded as an additional advantage of H_2O as an abundance indicator of oxygen in M dwarfs.

Fig. 13: The major species of carbon and oxygen in the photospheres of M dwarfs (p.24).

6.2. Oxygen Abundances in M Dwarfs

We take the weighted mean (with the numbers of lines used as weights) of the oxygen abundances resulting from the analyses of the regions A (section 4) and B (section 5) for 20 M dwarfs for which the two regions have been analyzed. The results and those from the region A alone (18 objects) are summarized in Table 8 together with the carbon abundances from Paper I. Also, the classical and more recent solar carbon and oxygen abundances by Anders & Grevesse (1989) and Asplund et al. (2009), respectively, are included in Table 8 for comparison.

The resulting values of $\log A_{\rm O}$ are plotted against the values of $\log A_{\rm C}$ in Fig. 14. The larger filled circles are based on the mean oxygen abundances from the regions A and B while the smaller filled circles from the region A alone. The two representative solar values are shown by $\odot$ marks. The initial assumed values of $\log A_{\rm O} = \log A_{\rm C} + 0.30$ are represented by the solid line in Fig. 14. The oxygen abundances are systematically lower than the assumed initial values in the carbon-rich M dwarfs. This tendency can be shown more clearly by plotting the values of $\log A_{\rm O}/A_{\rm C}$ (given in the fourth column of Table 8) against the values of $\log A_{\rm C}$ as illustrated in Fig. 15. Clearly abundances of oxygen relative to carbon are systematically smaller in M dwarfs with the larger carbon abundances. This result agrees well with the result by Gustafsson et al. (1999) who have determined carbon abundances in 80 F and G dwarfs (and oxygen abundances from Edvardsson et al. 1993) in the larger metallicity range with the use of the forbidden [CI] line, which is expected to be less sensitive to the photospheric structure and non-LTE effect compared to the other carbon abundance indicators for F and G dwarfs.

The carbon abundance may approximately represent the metallicity usually measured by the iron abundance. Then, Fig. 15 indicates that the $A_{\rm O}/A_{\rm C}$ ratios are larger at lower metallicities and gradually decrease in higher metallicities. Thus, Fig. 15 suggests different formation histories of carbon and oxygen in the evolution of the Galaxy. After the large production of oxygen by Type

II supernovae/hypernovae in the early Galaxy, the decrease of oxygen and carbon with increasing metallicity in the metallicity range of Fig.15 is due to Type I supernovae which produce more iron, but the decrease of carbon may be tempered by the contribution of carbon from AGB stars (Nomoto et al. 2013). However, the actual site of carbon production is still unclear as discussed in detail by Gustafsson et al. (1999). In view of the advantage of CO and H_2O as abundance indicators of carbon and oxygen, respectively, as noted in the previous subsection, the systematic decrease of the O/C ratios at the higher metallicities found in M dwarfs would provide the best observational constraint on the formation of carbon and oxygen in the chemical evolution of the Galactic disk.

We have shown in Paper I (see its Fig. 15) that the solar carbon abundance is atypical for its metallicity compared to the M dwarfs in the solar neighborhood if the recently downward revised solar value (Allende Prieto et al. 2002) is adopted. To examine the case of oxygen, we summarize the metallicities [Fe/H] = $\log A^{*}_{\rm Fe}$ - $\log A^{\odot}_{\rm Fe}$ from the literature (Mould 1978; Önehag et al. 2012; Neves et al. 2013) in Table 9. The iron abundances $\log A_{\rm Fe}$ are obtained assuming solar value of $\log A^{\odot}_{\rm Fe}$ = -4.5 (Asplund et al. 2009) and, together with our oxygen abundances, O/Fe ratios are obtained. The resulting values of $\log A_{\rm O}/A_{\rm Fe}$ are plotted against [Fe/H] in Fig. 16. Except for a few case, O/Fe ratios show a systematic increase towards lower [Fe/H], confirming the well known excess production of oxygen in metal-poor era. The two solar results are shown by the $\odot$ marks: The higher O/Fe case (marked with 1) is based on the classical solar abundance (Anders & Grevesse 1989) and the O/Fe ratio follows the general trend shown by the M dwarfs. To the contrary, the lower O/Fe ratio (marked with 2) based on the recent downward revised oxygen abundance (Asplund et al. 2009) does not follow the general trend shown by the M dwarfs, or the solar oxygen abundance is atypical for its metallicity compared with the nearby M dwarfs which is typical unevolved stars in the Galactic disk. On the other hand, it was shown that the solar abundances including oxygen are typical for its metallicity, compared to the elemental abundances in unevolved stars in the solar neighborhood (Edvardsson et al. 1993). The classical solar oxygen abundance (Anders & Grevesse 1989) is consistent with this result while the downward revised result (Allende Prieto et al. 2002; Asplund et al. 2009) is contradicting with this result.

So far, evolution of chemical elements in the Universe has been studied mostly from the abundance analyses of G type dwarfs including the halo sample, and there should be some reasons for this choice. For example, these stars are relatively well understood with the Sun as the prototype compared to very hot and very cool stars and, especially, many metallic lines used for abundance analysis can be observed in their spectra. However, one drawback to use G type dwarfs as tracers of the chemical history of the Galaxy, is that the photospheres of these stars may possibly be polluted by accretion of the metal-rich matter through encounter with the interstellar gas clouds during the evolution of the Galaxy, as has been pointed out first by Yoshii (1981). In this case, the accreted matter will not be diluted well because of the shallow convective zone in the G dwarfs, and the photospheric abundances will suffer appreciable changes from the values at their birth. Recently, observational support for this possibility has been presented by showing that the metallicity in halo G dwarfs is indeed larger by about 0.2 dex compared with that in K dwarfs of the same kinematic characteristics but having deeper convective zone (Hattori et al. 2014). Such a dilution effect may be most efficient in M dwarfs whose envelopes are wholly convective and the photospheric abundances may not be changed very much from the values at their birth. For this reason, M dwarfs could be the best tracers of the Galactic chemical evolution if chemical analysis can be extended to halo M dwarfs in the near future, and M dwarfs will provide unique contribution to our understanding on the element formation in the early Universe.

Finally, frequency distribution of oxygen abundances in 38 M dwarfs is shown in Fig. 17. The oxygen abundances $\log A_{\rm O}$ in M dwarfs are mostly between -3.5 and -3.0. On the other hand, a larger fraction of M dwarfs hosting planet(s) (those noted by ‡ in Table 8) are oxygen-rich, which is consistent with the results for carbon in Paper I and for metallicity in F, G, K, and M stars (e.g., Fischer & Valenti 2005; Johnson & Apps 2009).

Fig. 14: The logarithmic oxygen abundances $\log A_{\rm O}$ vs. $\log A_{\rm C}$ in 38 M dwarfs and the Sun (p.25).

Fig. 15: The values of $\log A_{\rm O}/A_{\rm C}$ plotted against $\log A_{\rm C}$ in 38 M dwarfs and the Sun (p.25).

Fig. 16: The values of $\log A_{\rm O}/A_{\rm Fe}$ plotted against [Fe/H] in 38 M dwarfs and the Sun (p.25).

Fig. 17: Frequency distribution of M dwarfs against $\log A_{\rm O}$ (p.25).

Table 8: Carbon and oxygen abundances in M dwarfs (p.34).

Table 9: Oxygen-to-Iron ratios in M dwarfs (p.34).

6.3. Method of Abundance Analysis

The spectra of cool stars including M dwarfs are apparently very complicated, and abundance analysis has been deemed difficult in general. We have done some trials in Paper I and in this paper to simplify the abundance analysis in M dwarfs, and we summarize our attempts.

In stellar abundance analysis, the so-called curve-of-growth (CG) method played an important role as detailed in the textbooks of classical astrophysics (e.g. Unsöld 1955). In its refined form, the so-called universal curve-of-growth, the growth of the equivalent width (EW) broadened by the Doppler and damping effects has been expressed in unified curves in dependence on the effective number of species producing the line. With this curve-of-growth, the observed EW could be transformed to the effective number of species and hence to the abundance of

element producing the line. This method has widely been applied to the stellar abundance determinations until the middle of the previous century. Despite the simplicity and wide applicability of the CG method, however, it has some drawbacks. For example, the effect of the photospheric structure could not be taken into account because of the simplified assumptions needed to compute EWs universally (i.e. for all the types of stars). Also, applications are limited to a single line with well defined profile which can be described by the Voigt profile.

To relax the problems in the CG method noted above, the so-called spectral synthesis (SS) method has been widely used in recent years. In this method, any model photosphere can be used in computing the synthetic spectrum including the blended features. Then the observed spectrum is compared with the predicted one characterized by several parameters including abundance, which are to be determined from the best fit between the observed and predicted spectra. Despite the wide use of the SS method, however, the stellar abundance determinations by different authors are still not well converged to a definite result (e.g., Lebzelter et al. 2012). One problem is that the different line-broadenings such as the rotation, micro- and macro-turbulence could not be separated on the synthetic spectrum. In this respect, the CG method has a definite advantage in that the EWs depend on the micro-turbulent velocity but not on the other line broadening, and thus micro-turbulence could be well separated from the other broadenings by the analysis of EWs with the CG method. Also, the SS as well as CG method is based on the prerequisite that the synthetic spectra as well as EWs are measured by referring to the true-continuum.

We believe that our analysis applied in subsection 4.1 has relaxed all the restrictions involved in the analyses noted above. As to the problem of continuum, we have noticed that the spectral analysis can be carried out by referring to the pseudo-continuum if it can be evaluated accurately on the theoretical spectrum, and recent progress in molecular database indeed makes such an approach possible (Paper I). Also, analysis is not limited to a single line but any blended features can be used. What is important is that the observed and theoretical spectral features are defined by exactly the same way by referring to the same reference (i.e., either the true- or pseudo-continuum). The abundance cannot directly be obtained from the observed EW of the spectral feature selected, but can be obtained easily with the use of a simple curve-of-growth. This CG is not necessary to cover the large range of EW as in the classical CG, but it should cover the restricted portion of the CG around the observed EW. Such a mini CG can be prepared theoretically by the use of EWs evaluated from the synthetic spectra including all the lines contributing to the spectral features to be analyzed. For this purpose, it is sufficient to generate three synthetic spectra for slightly different abundances, from which theoretical EWs are evaluated by exactly the same way as EW is measured on the observed spectrum. Then abundance can be obtained for the observed EW from the three-point mini CG. This analysis is repeated line-by-line or blend-by-blend for all the spectral features measured.

The mini CG method can best be applied to H_2O for which the pseudo-continuum level is also determined by H_2O itself. Then, the mini CG analysis directly provides the oxygen abundance. For comparison, in the case of CO discussed in Paper I, the pseudo-continuum level is determined not by CO itself but by H_2O and also EWs of CO measured include the contamination due to H_2O. For this reason, derived carbon abundance includes the effect of H_2O. Even though this effect is already included in the synthetic spectra from which EWs used for mini CG are evaluated, the result depends on the oxygen abundance assumed. For this reason, it is required to repeat the above processes by using the revised oxygen abundance if accurate result is required. In our Paper I, however, this process was skipped since the blending H_2O lines are rather weak and will have little effect.

The micro-turbulent velocity can be determined if necessary: For this purpose, we repeat the mini CG analysis with several assumed values of the micro-turbulent velocity. The resulting abundance corrections from different lines (or blends) depend little on the observed EWs only if the assumed micro-turbulent velocity is correct. In our analysis of M dwarfs, this requirement is almost satisfied for almost all the cases (see Figs. 5, 6, & 10) for the assumed micro-turbulent velocity, but this is because the thermal broadening dominates over the turbulent broadening as noted in subsection 6.1. If the turbulent broadening is dominating, the micro-turbulent velocity is determined so that the abundance corrections depend little on the observed EWs, and some examples are shown for the case of red giant stars using unblended lines (e.g., Tsuji 2008). It is still to be shown if the micro-turbulent velocity can be determined from the blended spectral features by the method outlined above.

We believe that our abundance analysis is essentially very simple and flexible enough to be easily applied to complicated blended spectra with depressed continuum, and we hope to have shown that the abundance analysis of cool stars is not especially difficult compared to that of other types of stars..

6.4. H_2O in Stellar Spectra other than M Dwarfs

We have shown that H_2O molecule can be an excellent abundance indicator of oxygen in M dwarfs. Then, we wonder if this is true for other types of stars including M type giants and supergiants which show H_2O lines in their spectra. For example, H_2O lines are prominent in the spectra of Mira type variables for which detailed spectroscopic analysis has been done by Hinkle & Barnes (1979), who showed that H_2O lines are composed of multiple components originating from different layers reflecting the complicated dynamical structures of their atmospheres. Then H_2O lines are primarily useful as the probes of the atmospheric structures of Mira type variables and abundance analysis would be more difficult.

Spectra of water vapor were observed in red giants and supergiants other than Mira type variables, but in the ways somewhat unexpected. For example, the announce-

ment to have detected H_2O lines in the early M supergiant Betelgeuse (α Ori, M2Iab) by Woolf et al. (1964) was so unexpected at that time that it could not be appreciated correctly for a long time (Tsuji 2000). Also, H_2O lines were observed in the K giant Arcturus (α Boo, K2IIIp) with high resolution in the atmospheric window near 12 μm (Ryde et al. 2002) and in the K giant Aldebaran (α Tau, K5III) with low resolution by ISO (Tsuji 2001). Such results are difficult to understand within the framework of the classical theory of stellar photospheres. Further, in non-Mira M giant stars, H_2O spectra were observed by ISO but showed excess absorption that could not be accounted for by the LTE model photospheres (e.g., Decin et al. 2003). Such problems must be solved before H_2O molecule can be used as an abundance indicator of oxygen in red giant and supergiant stars.

Probably the rarefied and extended atmospheres of high luminosity stars are more complicated to be described by the classical theory of stellar photospheres. Recent observations revealed that H_2O and CO are in fact found not in the photospheres but in the warm molecular layers extended out to $\approx 1.5\,R_*$ in M giant and supergiant stars (e.g., Ohnaka 2004; Montargès et al. 2014). Moreover, it was found recently from the aperture synthesis imaging of Betelgeuse that such molecular layers or clouds are asymmetrically extended and show large scale time-dependent dynamical structure (Ohnaka et al. 2011). Thus, interpretation of H_2O spectra in red giant and supergiant stars would require hybrid model atmosphere consisting of components with different dynamical characteristics, and H_2O spectra will serve primarily as probes of the outer atmospheric structure of high luminous cool stars.

7. Concluding Remarks

We have shown in the present paper and in Paper I that CO and H_2O spectra of M dwarfs can be excellent abundance indicators of carbon and oxygen, respectively, and carbon and oxygen abundances in dozens of M dwarf stars have been determined rather well. This conclusion may appear to be somewhat unexpected in view of the difficulties so far experienced in the attempts to analyze the spectra of M dwarfs. However, a new possibility of determining chemical abundances in cool dwarf stars has been opened by the recent progress as follows:

First, the progress in observations is remarkable. For examples, infrared spectra of high quality can be obtained by the use of new infrared detectors, fundamental parameters such as the effective temperatures are determined from the directly measured angular diameters, and high precision photometric and astrometric data on M dwarfs are available especially from the space observations.

Second, the traditional abundance analysis appears to be difficult in M dwarfs whose continuum levels are depressed by the numerous molecular lines. However, given that the pseudo-continuous levels defined by the numerous molecular lines can be evaluated accurately with the use of the recent molecular database, spectral analysis referring to the pseudo-continuum results in an identical result with that referring to the true-continuum, as we have shown in the present paper.

Third, abundance analysis depends on model photospheres, which are unfortunately by no means perfect yet because of the extreme complexity of the real photospheres. For this reason, it is useful to do abundance analysis to be free from imperfect modelling of the photospheric structure as far as possible. In the photospheres of M dwarfs, CO abundance is identical with the abundance of carbon itself in almost all the M dwarfs and H_2O abundance is almost the same with $A_O - A_C$ except for early M dwarfs (subsection 6.1). Then, CO and H_2O abundances depend little on the model applied. For this reason, carbon and oxygen abundances can best be determined in M dwarfs rather than in other types of stars.

Thanks to the favorable conditions noted above, the abundance analysis of M dwarfs based on CO and H_2O has been done rather well within the framework of the classical LTE analysis. This shows a marked contrast to the case of molecular spectra in high luminous cool stars including K - M giant and supergiant stars, in which classical LTE analysis encountered serious difficulties (subsection 6.4). As expected, LTE analysis is applicable to the high density and compact photospheres of low luminous stars rather than to the low density and extended atmospheres of high luminous stars. Although we certainly hope that the analysis of molecular spectra can be done consistently both in low and high luminous stars in the near future, we now take the advantage that the spectra of M dwarfs can be analyzed on the basis of the well established classical theory of spectral line formation, and we hope that M dwarfs will be used more widely as the probes of the chemical abundances in the Universe.

We thank an anonymous referee for careful reading of the text, and for providing many helpful suggestions that contributed to clarification and better presentation of our result.

This research makes use of data products from the Wide-field Infrared Survey Explorer which is a joint project of the University of California, Los Angeles, and the Jet Propulsion Laboratory / California Institute of Technology, funded by NASA.

This research has made use of the VizieR catalog access tool and the SIMBAD database, both operated at CDS, Strasbourg, France, and of the RECONS database in www.recons.org.

Computations are carried out on common use data analysis computer system at the Astronomy Data Center, ADC, of the National Astronomical Observatory of Japan.

Appendix 1. The AllWISE vs. the WISE All-Sky Catalogs

The absolute magnitudes at 3.4 μm, $M_{3.4}$, based on the WISE $W1$ fluxes given in the AllWISE Catalog are shown in Tables 10 and 11, while those in the WISE All-Sky Release were shown in Tables 3 and 4 of Paper I. The $M_{3.4} - \log T_{\rm eff}$ plots based on the data in Tables 10 and 11

are illustrated in Fig. 18 and the dashed line is the exact copy from that given in Fig. 1 of Paper I. As noted in section 2, the dashed line fits the plots in Fig. 18 quite well, and can be applied to the data of both the AllWISE and the WISE All Sky Catalogs.

Fig. 18: The absolute magnitude $M_{3.4}$ based on the AllWISE Catalog plotted against $\log T_{\rm eff}$ (p.26).

Table 10: $M_{3.4}$ and $T_{\rm eff}$ based on the interferometry (p.35).

Table 11: $M_{3.4}$ and $T_{\rm eff}$ based on the infrared flux method (p.35).

References

Allende Prieto, C., Lambert, D. L., & Asplund, M. 2002, ApJ, 573, L137
Anders, E., & Grevesse, N. 1989, Geochim. Cosmochim. Acta, 53, 197
Asplund, M., Grevesse, N., Sauval, A. J., & Scott, P. 2009, ARA&A, 47, 481
Auman, J. R. 1967, ApJS, 14, 171
Auman, J. R. 1969, in Low-Luminosity Stars ed. S. S. Kumar (New York: Gordon and Breach Sci. Publ.), 483
Barber, R. J., Tennyson, J., Harris, G. J., & Tolchenov, R. N. 2006, MNRAS, 368, 1087
Bean, J. L., Sneden, C., Hauschildt, P. H., Johns-Krull, C. M., & Benedit, G. F. 2006, ApJ, 652, 1604
Bernath, P. F. 2002, Phys. Chem. Chem. Phys., 4, 1501
Berriman, G., & Reid, N. 1987, MNRAS, 227, 315
Biémont, E., Baudoux, M., Kurucz, R. L., Ansbacher, W., & Pinnington, E. H. 1991, A&A, 249, 539
Boyajian, T. S., et al. 2012, ApJ, 757, 112
Connes, P. 1970, ARA&A, 8, 209
Cox, A. N. (ed.) 1999, Allen's Astrophysical Quantities, Fourth Edition (Berlin: Springer-Verlag), 145
Decin, L., Vandenbussche, B., Waelkens, C., Decin, G., Eriksson, K., Gustafsson, B., Plez, B., & Sauval, A. J. 2003, A&A, 400, 709
Edvardsson, B., Andersen, J., Gustafsson, B., Lambert, D. L., Nissen, P. E., & Tomkin, J. 1993, A&A, 275, 101
Faure, A., Wiesenfeld, L., Drouin, B. J., & Tennyson, J. 2013, JQSRT, 116, 79
Fischer, D. A., & Valenti, J. A. 2005, ApJ, 622, 1102
Gamache, R. R., Lynch, R., & Brown, L. R. 1996, JQSRT, 56, 471
Gliese, W., & Jahreiss, H. 1991, Preliminary Version of the Third Catalogue of Nearby Stars (Greenbelt: NASA/Astronomical Data Center)
Grevesse, N., & Sauval, A. J. 1999, A&A, 347, 348
Gustafsson, B., Karlsson, T., Olsson, E., Edvardsson, B., & Ryde, N. 1999, A&A, 342, 426
Hattori, K., Yoshii, Y., Beers, T., Carollo, D., & Lee, Y. S. 2014, ApJ, 784, 153
Herzberg, G. 1945, Molecular Spectra and Molecular Structure II. Infrared and Raman Spectra of Polyatomic Moleules (New York: D. Van Nostrand Co. Inc.), 207
Hinkle, K. H., & Barnes, T. G. 1979, ApJ, 227, 923
Holweger, H., Heise, C., & Kock, M. 1990, A&A, 232, 510
Johnson, J. A., & Apps, K. 2009, ApJ, 699, 933
Jones, H. R. A., Longmore, A. J., Jameson, R. F., & Mountain, C. M. 1994, MNRAS, 267, 413
Joy, A. H., & Abt, H. A. 1974, ApJS, 28, 1
Kessler, M. F., et al. 1996, A&A, 315, L27
King, G. W., Hainer, R. M., & Cross, P. C. 1943, J. Chem. Phys., 11, 27
Kobayashi, N., et al. 2000, Proc. SPIE, 4008, 1056
Kuiper, G. P. 1962, Comm. Lunar Planet. Lab., No.23, 179
Lebzelter, T., et al. 2012, A&A, 547, A108
Mohler, O. C. 1955, A Table of Solar Spectrum Wave Lengths 11984A to 25578A (Ann Arbor: The University of Michigan Press)
Montargès, M., Kervella, P., Perrin, G., Ohnaka, K., Chiavassa, A., Ridgway, S. T., & Lacour, S. 2014, A&A, 572, A17
Mould, J. R. 1978, ApJ, 226, 923
Neves, V., Bonfils, X., Santos, N. C., Delfosse, X., Forveille, T., Allard, F., & Udry, S. 2013, A&A, 551, A36
Nomoto, K., Kobayashi, C., & Tominaga, N. 2013, ARA&A, 51, 457
Ohnaka, K. 2004, A&A, 421, 1149
Ohnaka, K., et al. 2011, A&A, 529, A163
Önehag, A., Heiter, U., Gustafsson, B., Piskunov, N., Plez, B., & Reiners, A. 2012, A&A, 542, A33
Polyansky, O. L., Zobov, N. F., Viti, S., Tennyson, J., Bernath, P. F., & Wallace, L. 1997, ApJ, 489, L205
Ridgway, S. T., & Brault, J. W. 1984, ARA&A, 22, 29
Rothman, L. S., et al. 2010, JQSRT, 111, 2139
Russell, H. N. 1934, ApJ, 79, 317
Ryde, N., Lambert, D. L., Richter, M. J., & Lacy, J. H. 2002, ApJ, 580, 447
Steyert, D. W., Wang, W. F., Sirota, J. M., Donahue, N. M., & Reuter, D. C. 2004, JQSRT, 83, 183
Struve, O., & Elvey, C. T. 1934, ApJ, 79, 409
Tereszchuk, K., Bernath, P. F., Zobov, N. F., Shirin, S. V., Polyansky, O. L., Libeskind, N. I., Tennyson, J., & Wallace, L. 2002, ApJ, 577, 496
Tinney, C. G., Mould, J. R., & Reid, I. N. 1993, AJ, 105, 1045
Tsuji, T. 1966, PASJ, 18, 127
Tsuji, T. 1969, in Low-Luminosity Stars ed. S. S. Kumar (New York: Gordon and Breach Sci. Publ.), 457
Tsuji, T. 2000, ApJ, 538, 801
Tsuji, T. 2001, A&A, 376, L1
Tsuji, T. 2002, ApJ, 575, 264
Tsuji, T. 2005, ApJ, 621, 1033
Tsuji, T. 2008, A&A, 489, 1271
Tsuji, T., & Nakajima, T. 2014, PASJ, 66, 98 (Paper I)
Tsuji, T., Ohnaka, K., & Aoki, W. 1996, A&A, 305, L1
Unsöld, A. 1955, Physik der Sternatmosphären mit Besonderer Berücksichtigung der Sonne, 2ten Auf. (Berlin: Springer-Verlag)
van Leeuwen, F. 2007, A&A, 474, 653
von Braun, K., et al. 2014, MNRAS, 438, 2413
Wallace, L., Bernath, P., Livingston, W., Hinkle, K., Busler, J., Guo, B., & Zhang, K. 1995, Science, 268, 1155
Wallace, L., & Livingston, W. 1992, N. S. O. Technical Report No.92-001, An Atlas of a Dark Sunspot Umbral Spectrum in the Infrared from 1970 to 8640 cm^{-1} (Tucson: NOAO)
Woolf, N. J., Schwarzschild, M., & Rose, W. K. 1964, ApJ, 140, 833
Wright, E. L., et al. 2010, AJ, 140, 1868
Yoshii, Y. 1981, A&A, 97, 280
Zobov, N. F., et al. 2000, ApJ, 530, 994
Zobov, N. F., et al. 2008, MNRAS, 387, 1093

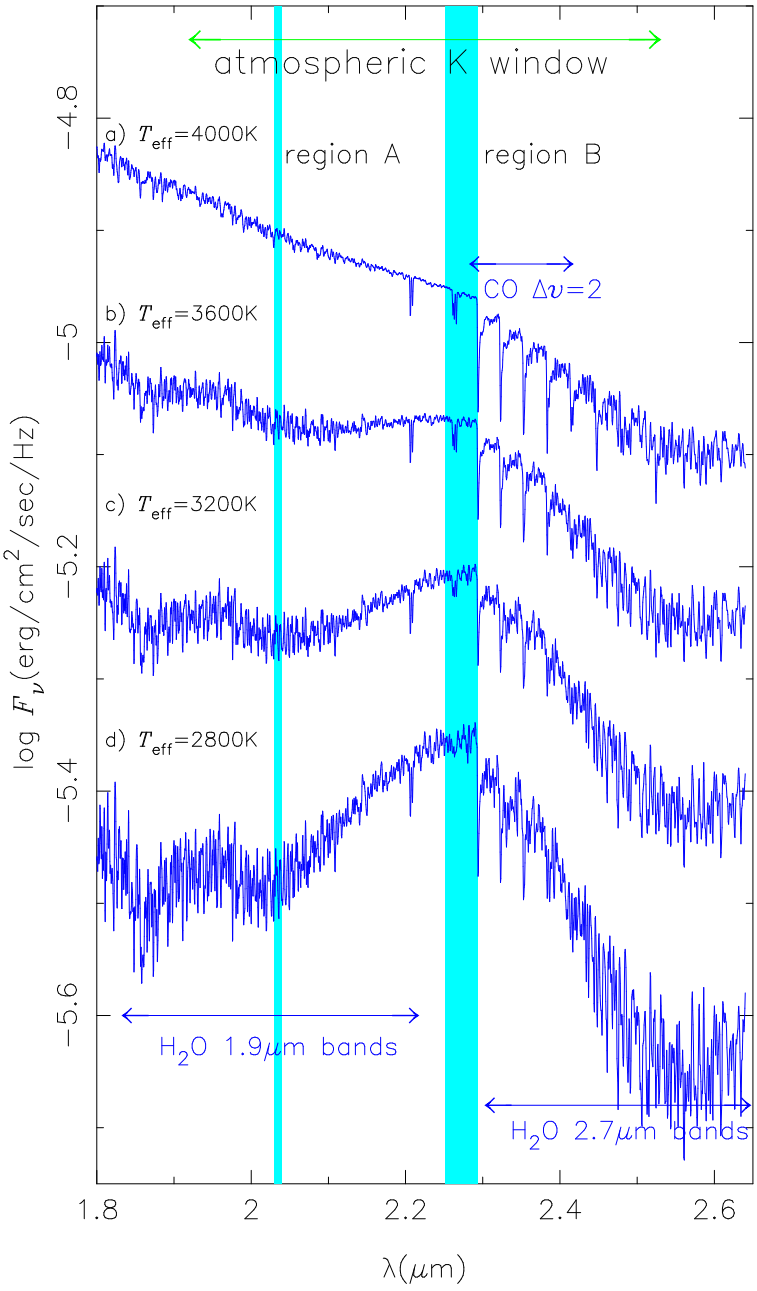

Fig. 1. Spectra of M dwarfs ($R = 2000$) in the K band region based on the model photospheres of $T_{\rm eff}/\log g$ = a) 4000 K/4.5, b) 3600 K/4.75, c) 3200 K/5.0, and d) 2800 K/5.25. The H_2O 1.9 and 2.7 μm bands are increasingly stronger in cooler models, but the CO second overtone bands are rather masked by H_2O bands in the cooler models. The regions A and B, which are in the atmospheric window shown at the top of the figure, are selected for detailed analysis of H_2O lines. The region A is in the midst of H_2O 1.9 μm bands while the region B suffers the effects of both the H_2O 1.9 and 2.7 μm bands least.

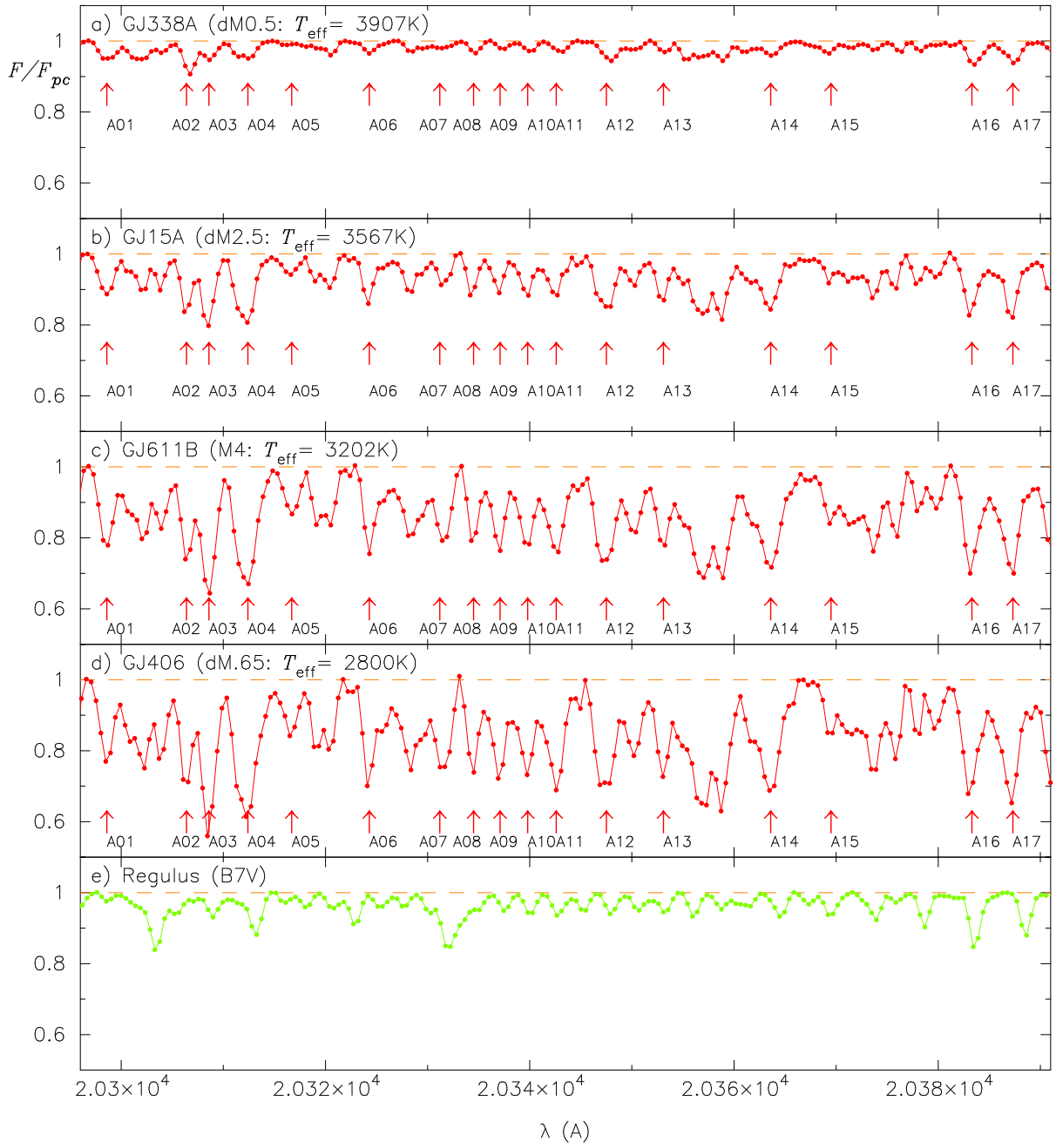

Fig. 2. The spectra of M dwarfs in the region A roughly in the order of the decreasing effective temperatures: a) GJ 338A, b) GJ 15A, c) GJ 611B, and d) GJ 406. Also shown is e) Regulus used for calibration. The candidates of H_2O blends for detailed analysis are indicated by arrows with the reference numbers A01–A17 to Tables 2 & 3.

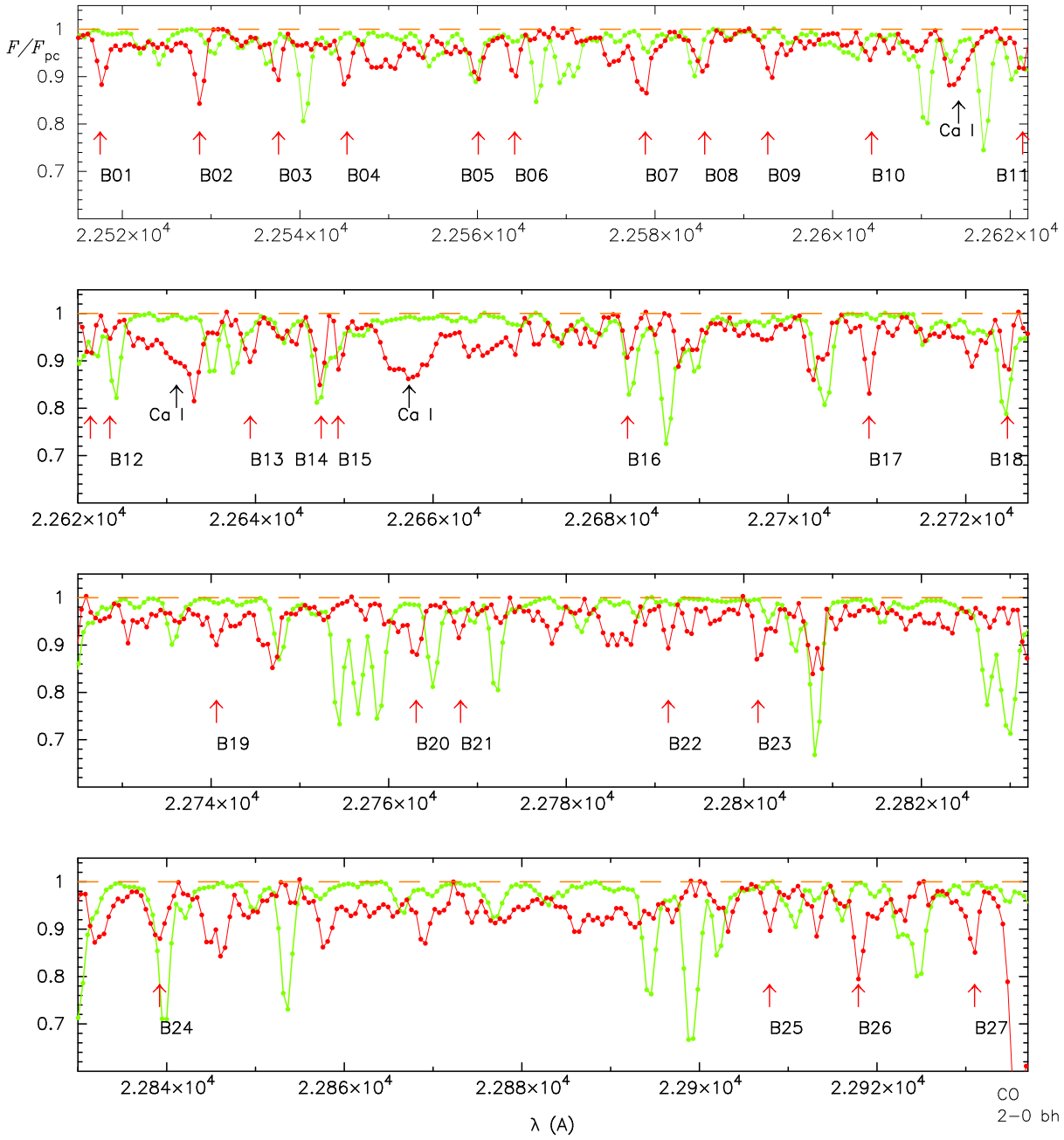

Fig. 3. The spectrum of GJ 406 (red or black) as an example of the spectrum in the region B. The spectrum of Regulus (green or grey) is used as the calibrator of the wavelength and the atmospheric absorption. The candidates of H_2O blends for detailed analysis are indicated by arrows with the reference numbers B01–B27 to Tables 4 & 5. The strong lines in Regulus are CH_4 and N_2O of telluric origins.

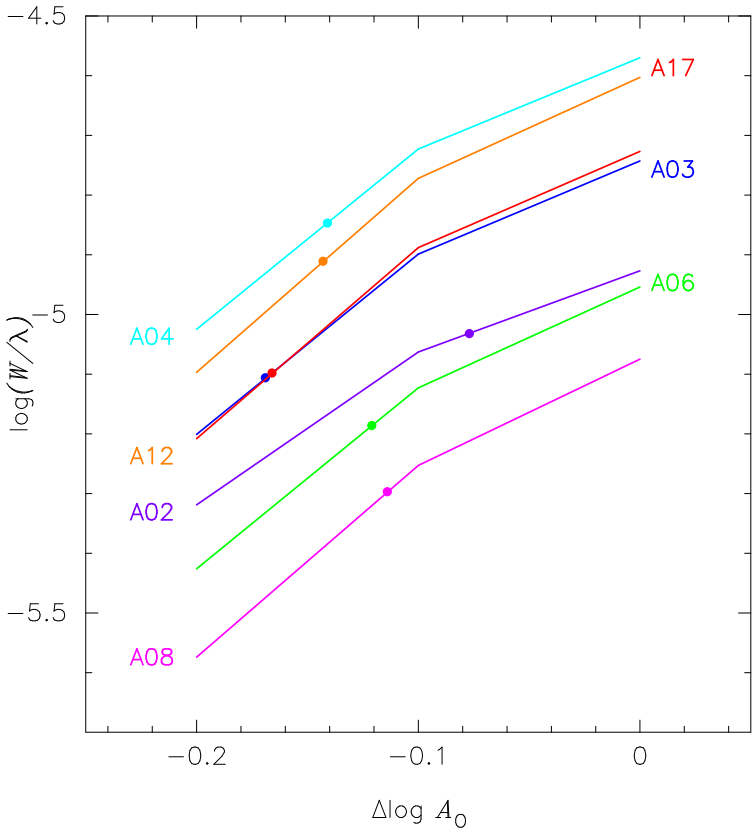

Fig. 4. Mini curves-of-growth for seven selected H_2O blends in GJ 229, and the reference numbers to Table 3 are shown for the corresponding mini CG. The filled circle on each mini curve-of-growth indicates the observed value of $\log(W/\lambda)_{\rm obs}$ (from Table 3 and read on the ordinate) and the resulting value of the abundance correction $\Delta\log A_{\rm O}$ (read on the abscissa and plotted on Fig 5d by filled circle).

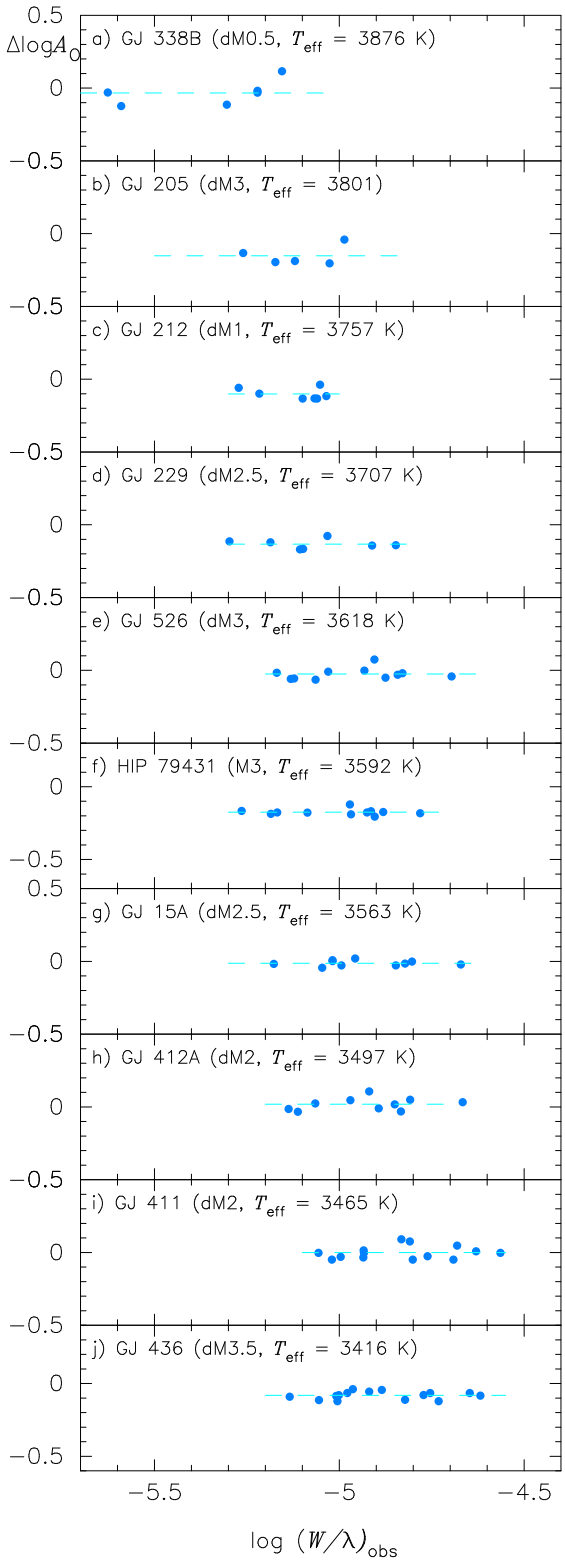
a) GJ 338B (dM0.5, $T_{\rm eff}$ = 3876 K)
b) GJ 205 (dM3, $T_{\rm eff}$ = 3801)
c) GJ 212 (dM1, $T_{\rm eff}$ = 3757 K)
d) GJ 229 (dM2.5, $T_{\rm eff}$ = 3707 K)
e) GJ 526 (dM3, $T_{\rm eff}$ = 3618 K)
f) HIP 79431 (M3, $T_{\rm eff}$ = 3592 K)
g) GJ 15A (dM2.5, $T_{\rm eff}$ = 3563 K)
h) GJ 412A (dM2, $T_{\rm eff}$ = 3497 K)
i) GJ 411 (dM2, $T_{\rm eff}$ = 3465 K)
j) GJ 436 (dM3.5, $T_{\rm eff}$ = 3416 K)
$\Delta\log A_{\rm O}$
$\log\ (W/\lambda)_{\rm obs}$

Fig. 5. The resulting logarithmic abundance corrections $\Delta\log A_{\rm O}$ by the mini curves-of-growth analysis for the H_2O blends in the region A are plotted against the observed values of $\log(W/\lambda)_{\rm obs}$. The dashed line shows the mean value of $\Delta\log A_{\rm O}$. In this figure, relatively early M dwarfs are shown in the order of decreasing effective temperatures.

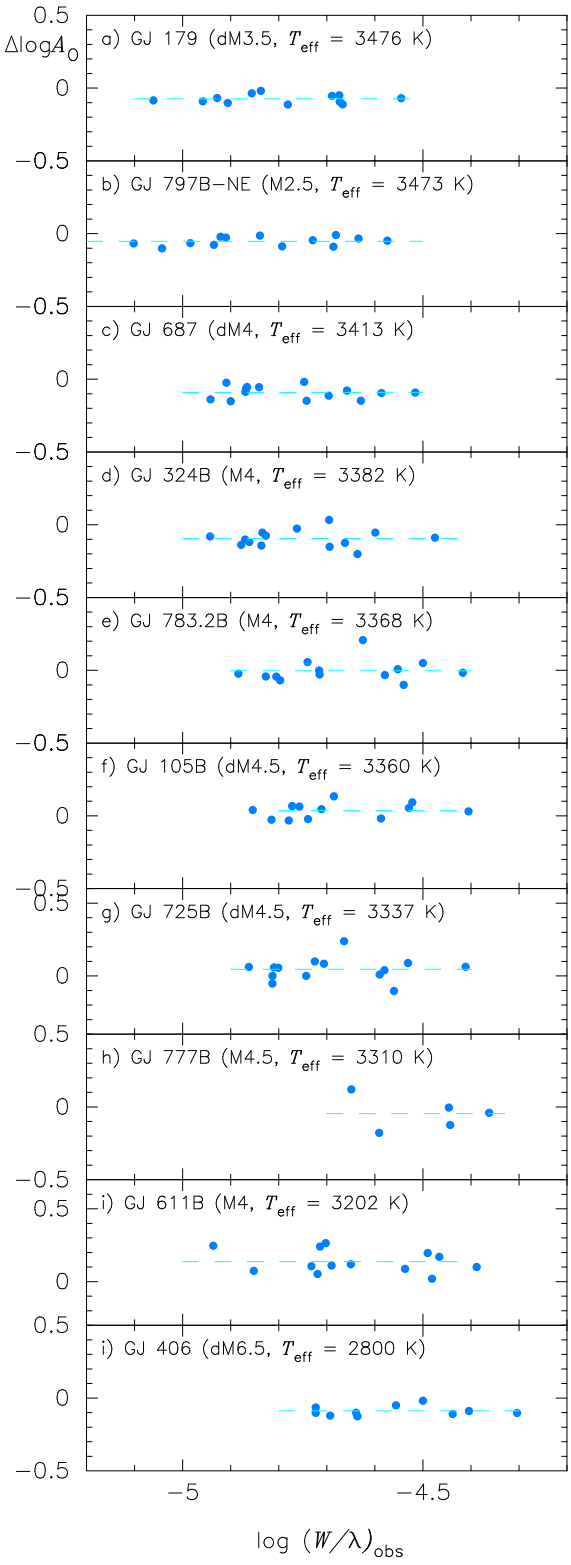
a) GJ 179 (dM3.5, $T_{\rm eff}$ = 3476 K)
b) GJ 797B–NE (M2.5, $T_{\rm eff}$ = 3473 K)
c) GJ 687 (dM4, $T_{\rm eff}$ = 3413 K)
d) GJ 324B (M4, $T_{\rm eff}$ = 3382 K)
e) GJ 783.2B (M4, $T_{\rm eff}$ = 3368 K)
f) GJ 105B (dM4.5, $T_{\rm eff}$ = 3360 K)
g) GJ 725B (dM4.5, $T_{\rm eff}$ = 3337 K)
h) GJ 777B (M4.5, $T_{\rm eff}$ = 3310 K)
i) GJ 611B (M4, $T_{\rm eff}$ = 3202 K)
i) GJ 406 (dM6.5, $T_{\rm eff}$ = 2800 K)
$\Delta\log A_{\rm O}$
$\log\ (W/\lambda)_{\rm obs}$

Fig. 6. The same as in Fig. 5 but for later M dwarfs in the order of decreasing effective temperatures.

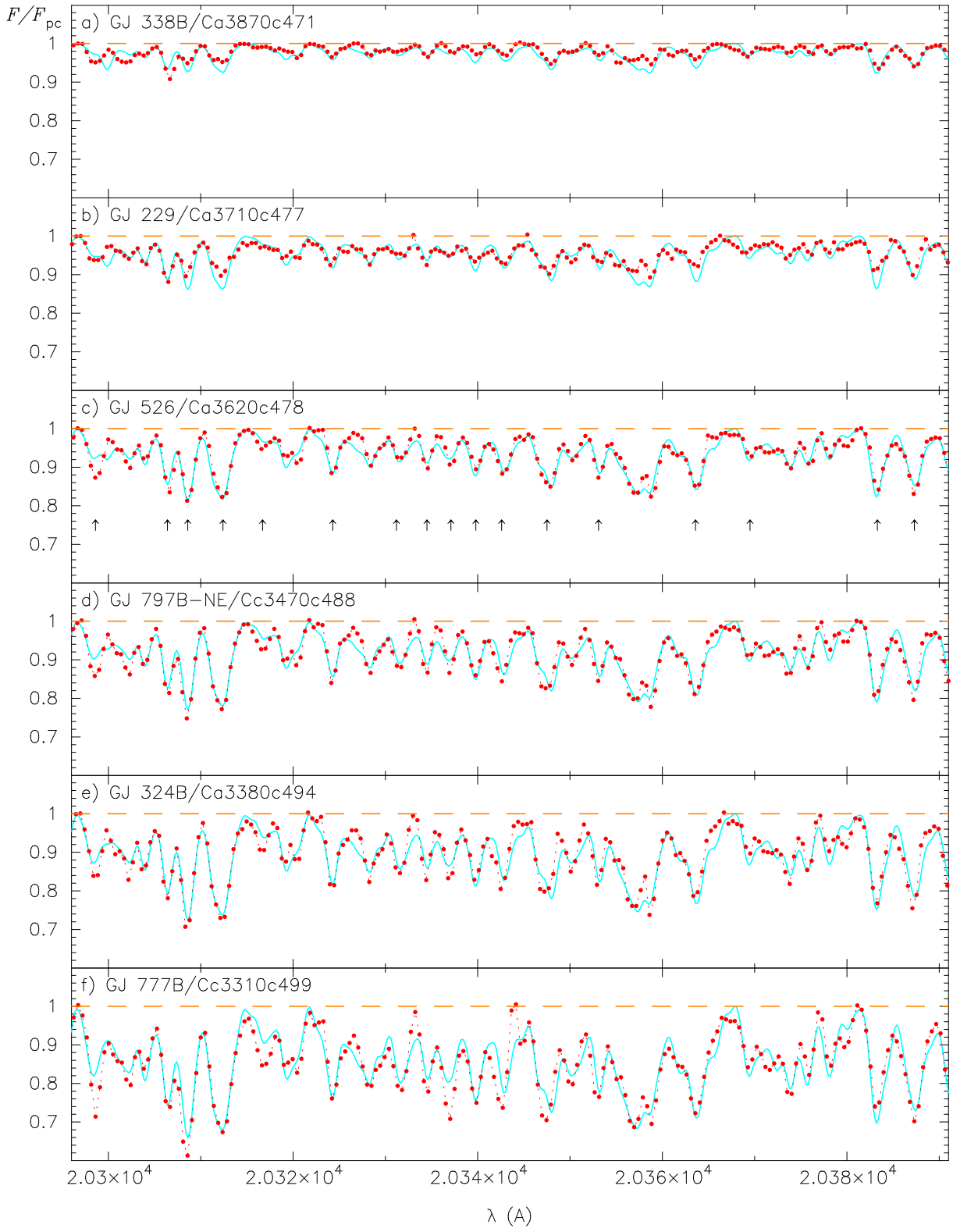

Fig. 7. Comparison of the observed (filled circles) and predicted (solid lines) spectra based on the oxygen abundances $\log A_{\rm O}^{\rm A}$ in Table 6 for six selected M dwarfs: a) GJ 338B (dM0.5) . b) GJ 229 (dM2.5). c) GJ 526 (dM3). d) GJ 797B-NE (M2.5). e) GJ 324B (M4). f) GJ 777B (M4.5).

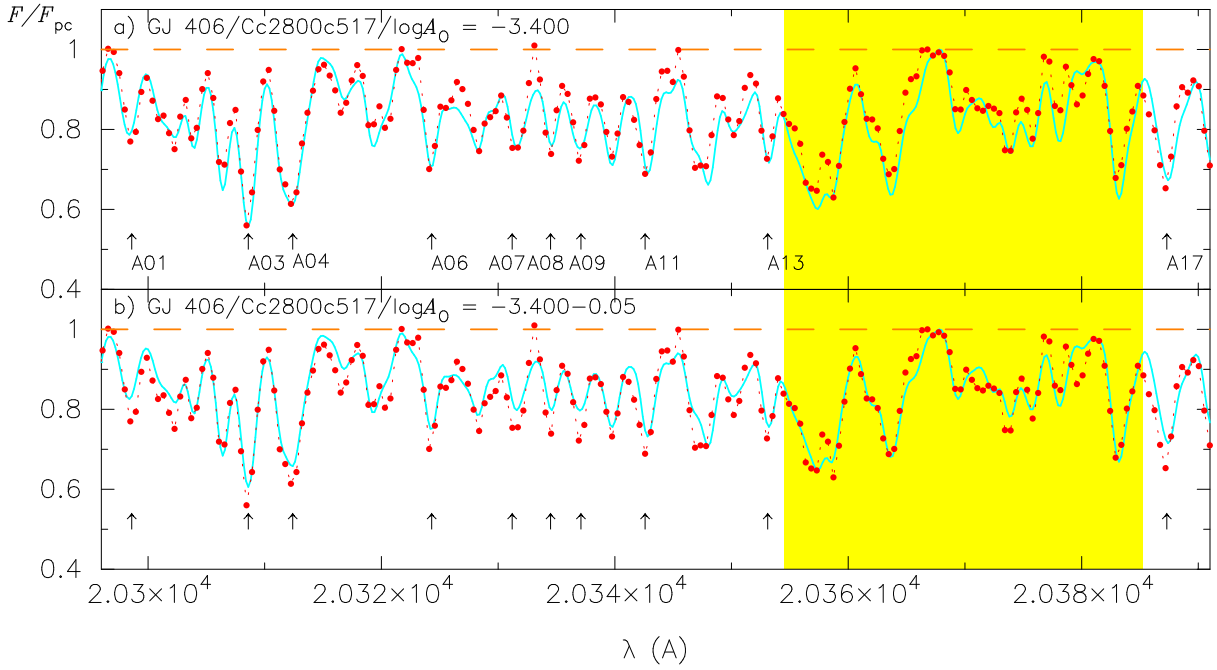

Fig. 8. Comparison of the observed (filled circles) and predicted (solid lines) spectra for GJ 406: a) For the oxygen abundance $\log A_O$ = -3.40 in Table 6 resulting χ^2 = 13.204, but fittings are fine for the blends used for the analysis (indicated by the arrows). b) For the oxygen abundance $\log A_O$ = -3.40 -0.05, resulting χ^2 = 10.510, but fittings are worse for the blends used for the analysis (indicated by the arrows). Then the part of the spectrum not used for the analysis (between 20354.2 and 20385.2Å; filled by yellow or grey in the figure) is excluded from the χ^2 test. The results are χ^2 = 11.119 and χ^2 = 11.227 for a) $\log A_O$ = -3.40 and b) $\log A_O$ = -3.40 -0.05, respectively, confirming that the mini CG analysis and the χ^2 analysis are consistent.

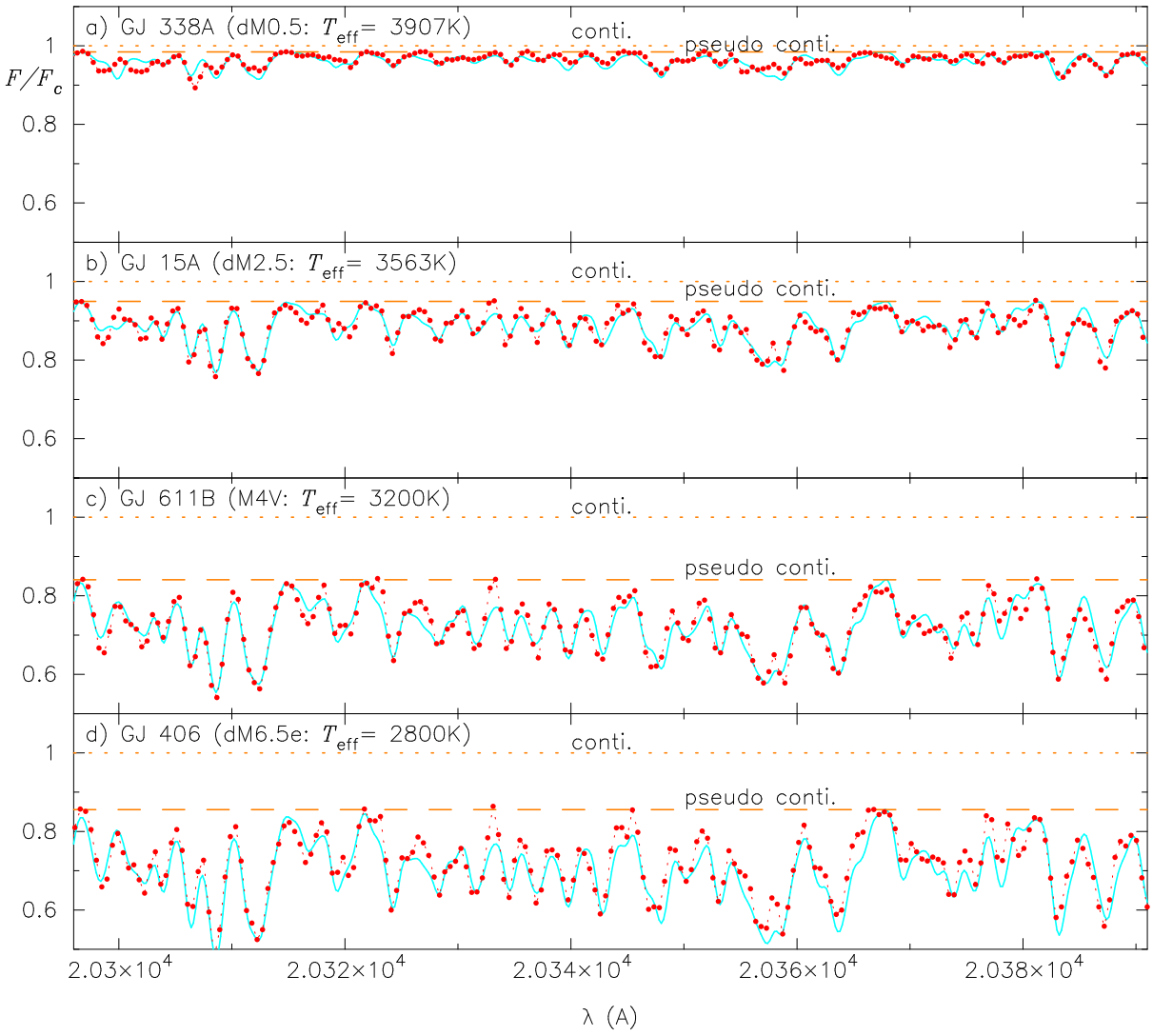

Fig. 9. Model spectra normalized by their true-continua shown by the dotted lines are shown by the solid lines for four model spectra. The observed spectra of the four stars normalized by their pseudo-continua (dashed lines) in Fig. 2 are shown here re-normalized by their true-continua estimated by applying the pseudo-to-true continua ratios of the model spectra. In this way, the depressions of the continuum levels of the four stars are estimated even though the true-continua can never be seen on the observed spectra.

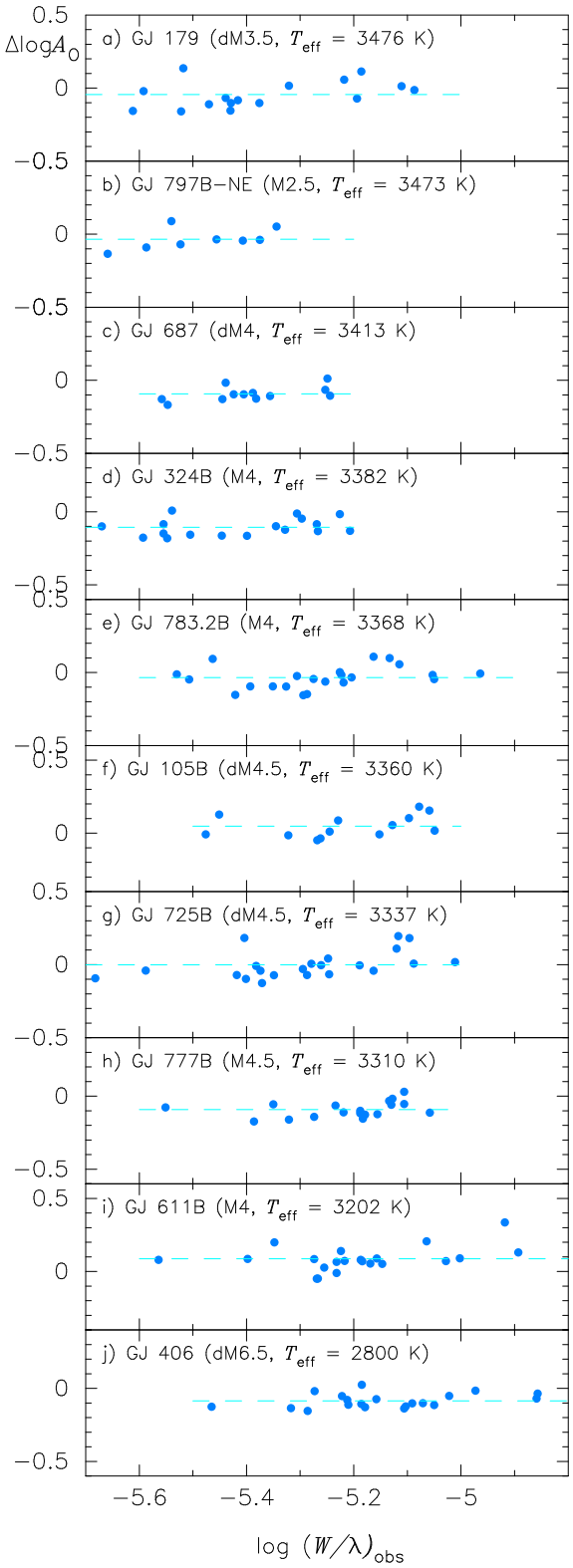
ΔlogA_O
a) GJ 179 (dM3.5, T_{eff} = 3476 K)
b) GJ 797B−NE (M2.5, T_{eff} = 3473 K)
c) GJ 687 (dM4, T_{eff} = 3413 K)
d) GJ 324B (M4, T_{eff} = 3382 K)
e) GJ 783.2B (M4, T_{eff} = 3368 K)
f) GJ 105B (dM4.5, T_{eff} = 3360 K)
g) GJ 725B (dM4.5, T_{eff} = 3337 K)
h) GJ 777B (M4.5, T_{eff} = 3310 K)
i) GJ 611B (M4, T_{eff} = 3202 K)
j) GJ 406 (dM6.5, T_{eff} = 2800 K)
0.5
0
−0.5
−5.6
−5.4
−5.2
−5
log $(W/\lambda)_{obs}$

Fig. 10. The resulting logarithmic abundance corrections $\Delta\log A_O$ by the mini curves-of-growth analysis for the H_2O blends in the region B plotted against the observed values of $\log(W/\lambda)_{obs}$. The dashed line shows the mean value of $\Delta\log A_O$. Compared with Fig. 6 for the same objects, larger numbers of blends can be used especially for later types.

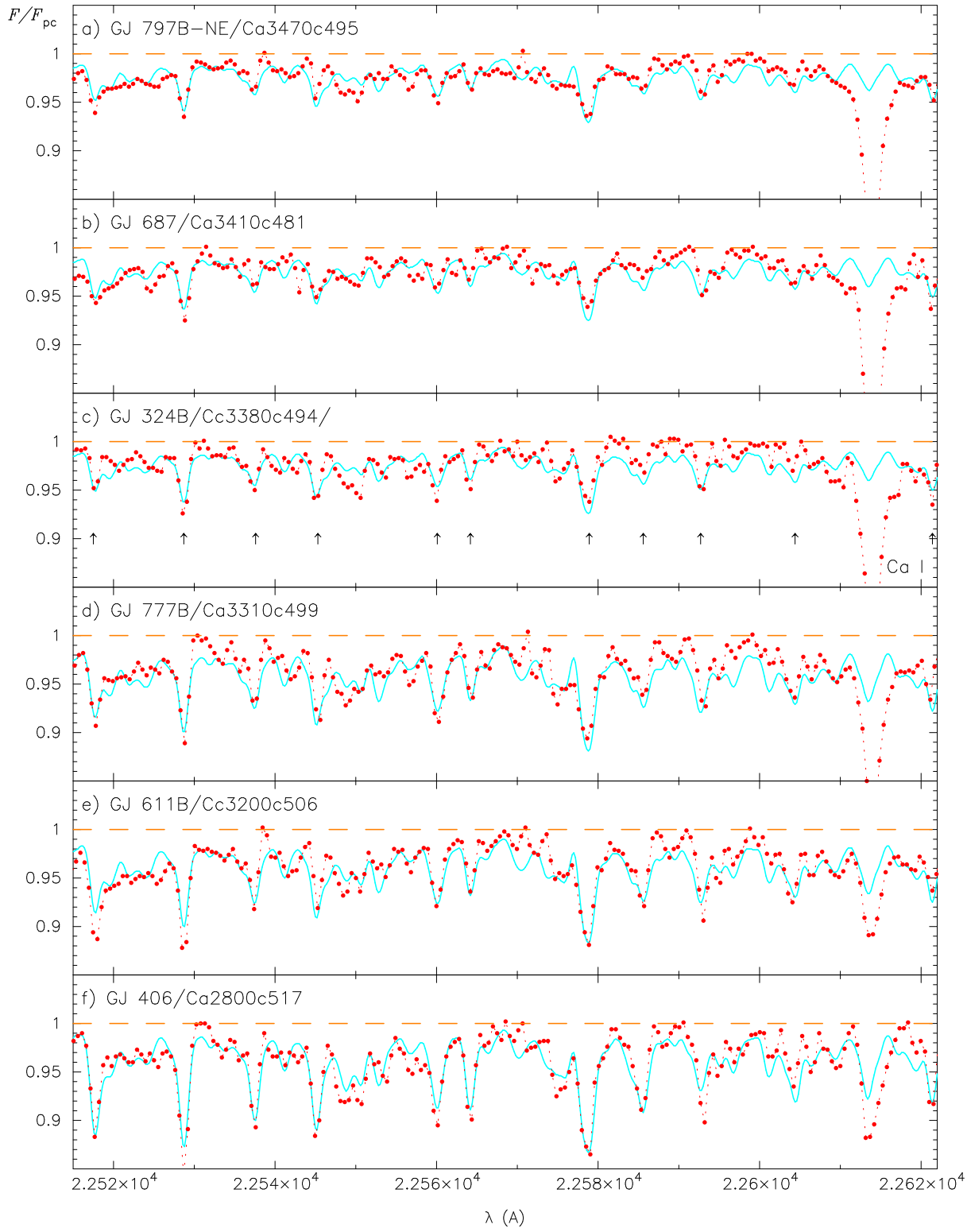

Fig. 11. Comparison of observed (filled circles) and predicted (solid lines) spectra based on the oxygen abundances determined from H_2O blends in the region B for six M dwarfs: a) GJ 797B-NE (M2.5). b) GJ 687 (dM4). c) GJ 324B (M4). d) GJ 777B (M4.5). e) GJ 611B (M4). f) GJ 406 (dM6.5). The strong feature at 22614 Å in each observed spectrum is due to Ca I line. But this Ca I line is not included in our line-list and the feature at the position of the Ca I line on the predicted spectra is not due to Ca but to H_2O.

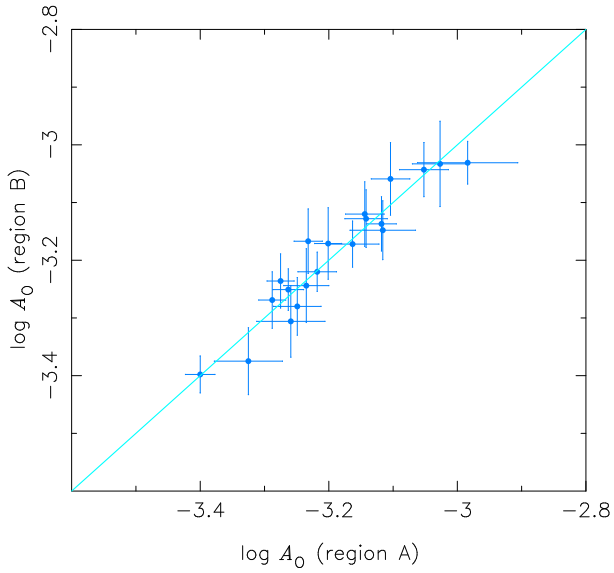

Fig. 12. Oxygen abundances determined from the region B are plotted against those from the region A. The results from the different regions agree within the probable errors in most objects.

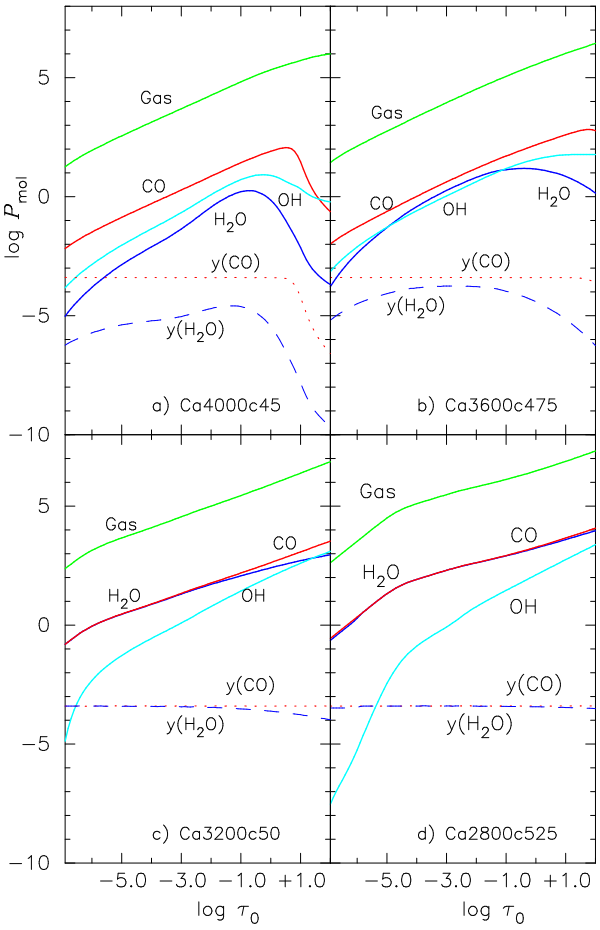

Fig. 13. Molecular abundances plotted against the optical depths in four model photospheres of $T_{\rm eff}/\log g$ = a) 4000 K/4.5, b) 3600 K/4.75, c) 3200 K/5.0, and d) 2800 K/5.25. Also, y(CO) and $y(\rm H_2O)$ are defined by equations (5) and (6), respectively, in the text. If almost all the carbon atoms are in CO (i.e., if CO is the major species of carbon), $y(\rm CO) \approx A_C$. If almost all oxygen atoms left after CO formation are in $\rm H_2O$ (i.e., if $\rm H_2O$ is the major species of oxygen), $y(\rm H_2O) \approx A_O - A_C$. It can be confirmed that CO is the major species of carbon in all the models and $\rm H_2O$ in the models of $T_{\rm eff} \lesssim 3400$ K.

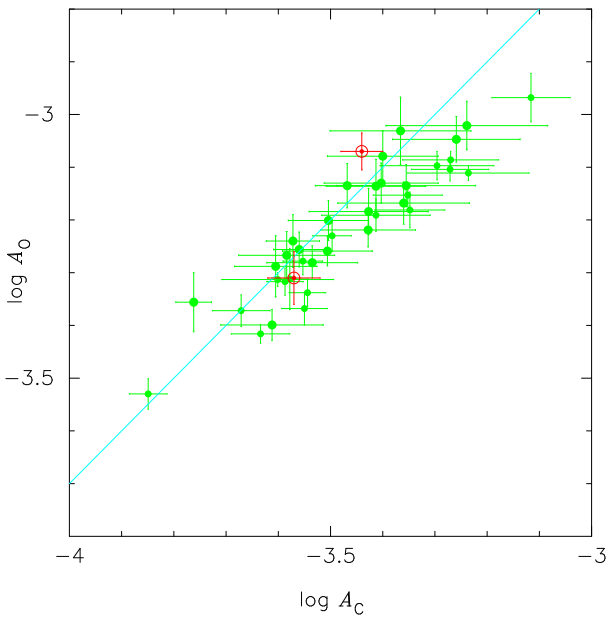

Fig. 14. The oxygen abundances $\log A_O$ are plotted against the carbon abundances $\log A_C$ in 38 M dwarfs. The classical high solar case is indicated by the upper ⊙ and the recent downward revised solar case by the lower ⊙. The assumed initial relation of $\log A_O = \log A_C + 0.30$ is shown by the sold line.

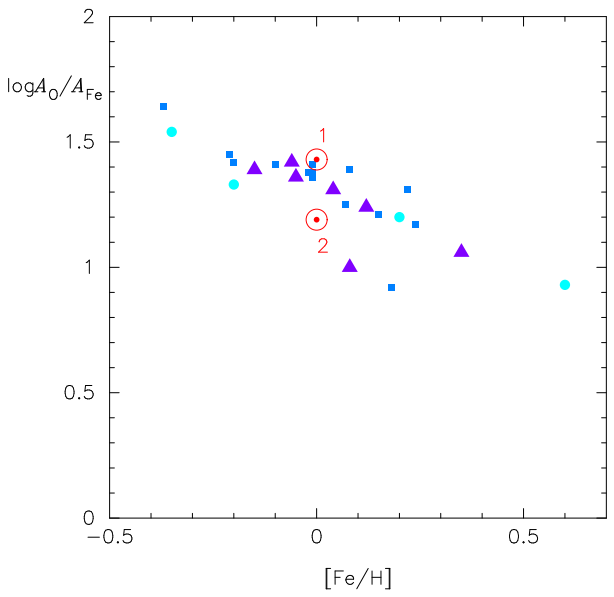

Fig. 16. The oxygen-to-iron ratios are plotted against [Fe/H] = $\log A^*_{Fe}$ - $\log A^{\odot}_{Fe}$ in M dwarfs and the Sun. The oxygen–to-iron ratio of the classical oxygen abundance (Anders & Grevesse 1989) follows the general trend shown by the M dwarfs (⊙ marked with 1), but that of the recent downward revised result (Asplund et al. 2009) does not follow the general trend (⊙ marked with 2). Thus, if the recently recommended low oxygen abundance is correct, the solar oxygen abundance is atypical for its metallicity.

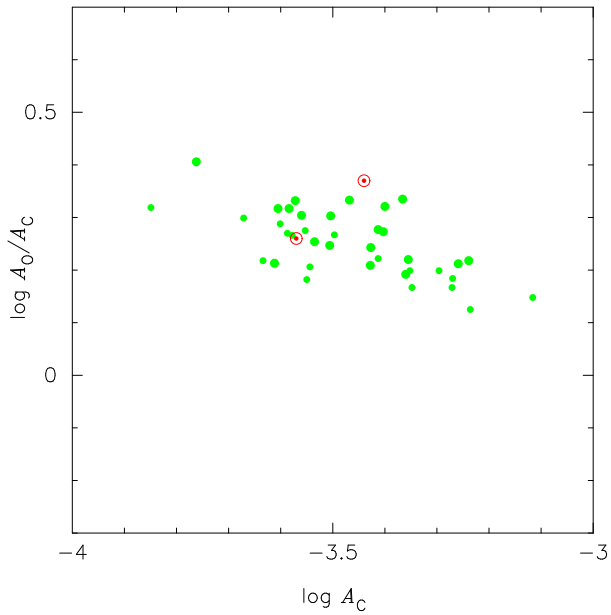

Fig. 15. The oxygen-to-carbon ratios are plotted against the carbon abundances $\log A_C$ in 38 M dwarfs, and in the Sun. The oxygen-to-carbon ratios are smaller at the higher carbon abundances, showing that carbon productions are more effective at higher metallicities.

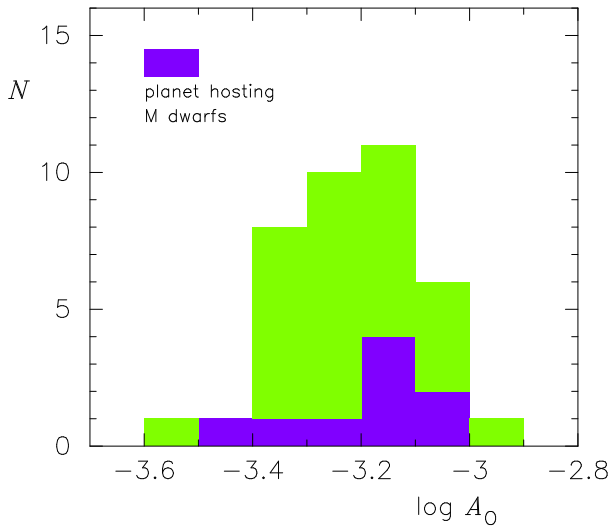

Fig. 17. Frequency distribution of M dwarfs against $\log A_O$. Note that nine M dwarfs are hosting planet(s).

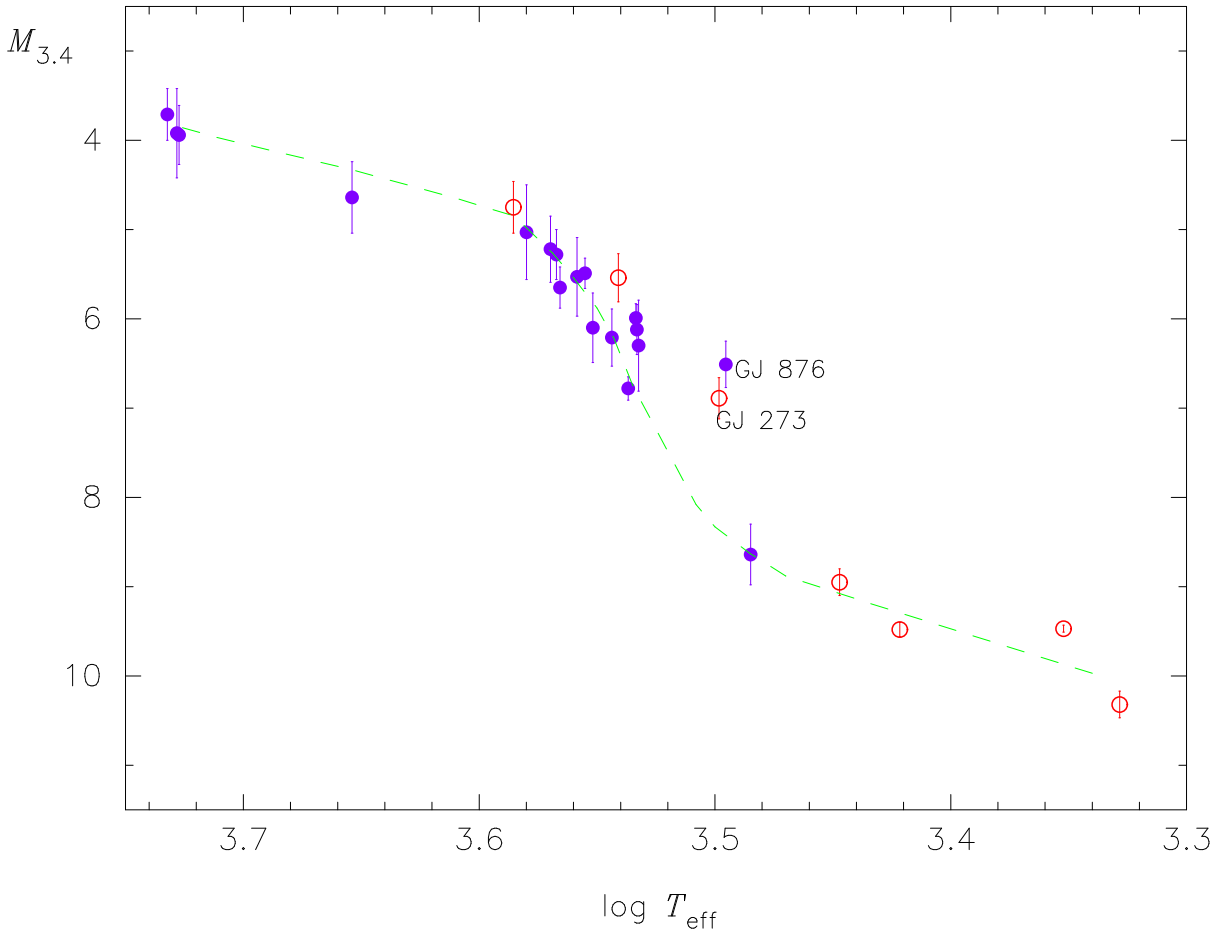

Fig. 18. The absolute magnitudes at 3.4 μm, $M_{3.4}$, plotted against $\log T_{\rm eff}$, where $M_{3.4}$ values are based on the AllWISE Catalog (see Tables 10 and 11) instead of the WISE All-Sky Catalog applied in Paper I. The probable errors of the AllWISE Catalog are larger than those of the WISE All-Sky Catalog in general. The values of $T_{\rm eff}$ based on the interferometry and infrared flux method are shown by the filled and open circles, respectively. The mean $M_{3.4}$ – $\log T_{\rm eff}$ relation shown by the dashed line is exactly the same as that in Fig. 1 of Paper I.

Table 1. Fundamental Parameters and Model Photospheres for the Program Stars.

obj.	Sp. Type*	$T_{\rm eff}$*	$\log g$*	model*
GJ 15A	dM2.5	3567	4.890	Ca3570c489
GJ 105B	dM4.5	3360	4.954	Ca3360c495
GJ 166C	dM4e	3337	4.972	Ca3340c497
GJ 176	dM2.5e	3616	4.804	Ca3620c480
GJ 179	dM3.5e	3476	4.877	Ca3480c488
GJ 205	dM3	3801	4.710	Ca3800c471
GJ 212	dM1	3757	4.748	Ca3760c475
GJ 229	dM2.5	3707	4.766	Ca3710c477
GJ 231.1B	M3.5	3442	4.897	Ca3440c490
GJ 250B	M2	3567	4.827	Ca3570c483
GJ 273	dM4	3415	4.915	Ca3420c492
GJ 324B	M4	3382	4.938	Ca3380c494
GJ 338A	dM0.5	3907	4.709	Ca3910c471
GJ 338B	dM0.5	3867	4.709	Ca3870c471
GJ 380	dM0.5	4081	4.643	Ca4080c464
GJ 406	dM6.5e	2800	5.170	Cc2800c517
GJ 411	dM2	3465	4.857	Cc3470c486
GJ 412A	dM2	3497	4.843	Cc3500c484
GJ 436	dM3.5	3416	4.797	Cc3420c480
GJ 526	dM3	3618	4.784	Cc3620c478
GJ 581	dM4	3442	4.959	Ca3440c496
GJ 611B	M4	3202	5.063	Cc3200c506
GJ 649	dM2	3660	4.784	Ca3660c478
GJ 686	dM1	3538	4.842	Ca3540c484
GJ 687	dM4	3413	4.811	Ca3410c481
GJ 725A	dM4	3407	4.837	Cc3410c484
GJ 725B	dM4.5	3337	4.972	Cc3340c497
GJ 768.1C	—	3470	4.881	Ca3470c488
GJ 777B	M4.5	3310	4.991	Ca3310c499
GJ 783.2B	M4	3370	4.949	Ca3370c495
GJ 797B-NE	M2.5	3473	4.878	Ca3470c488
GJ 797B-SW	M2.5	3473	4.878	Ca3470c488
GJ 809	dM2	3692	4.720	Ca3690c472
GJ 820B	dM0	3932	4.679	Ca3930c470
GJ 849	dM3.5	3580	4.821	Ca3580c482
GJ 876	dM4.5	3458	4.888	Ca3460c489
GJ 880	dM2.5	3713	4.716	Ca3710c472
GJ 884	dM0.5	3850	4.720	Ca3850c472
GJ 3348B	M4	3476	4.876	Ca3480c488
HIP 12961	M0	3890	4.709	Ca3890c471
HIP 57050	M4	3464	4.884	Ca3460c488
HIP 79431	M3	3592	4.815	Ca3590c482

* from Paper I.

Table 2. H_2O Lines in the Region A.

Ref.*	λ_{obs}†	λ†	$v_1' v_2' v_3'$	$v_1'' v_2'' v_3''$	J'	K_a'	K_c'	J''	K_a''	K_c''	log gf	L.E.P.‡
A01	20298.6	20298.213	1 0 1	0 1 0	15	8	8	16	8	9	-5.195	5949.217
		20298.428	0 3 2	0 2 1	9	3	7	10	3	8	-5.049	8358.617
		20298.838	0 1 1	0 0 0	19	11	9	20	11	10	-5.074	6664.142
A02	20306.4	20306.355	0 1 1	0 0 0	17	0	17	18	0	18	-5.284	3319.448
		20306.359	0 1 1	0 0 0	17	1	17	18	1	18	-4.676	3319.448
A03	20308.6	20308.271	0 1 1	0 0 0	16	6	10	17	6	11	-4.909	4291.907
		20308.479	0 2 1	0 1 0	15	5	11	16	5	12	-4.637	5310.240
		20308.775	0 2 1	0 1 0	14	4	10	15	4	11	-4.638	4894.586
A04	20312.4	20312.271	0 5 1	0 4 0	8	3	5	9	3	6	-4.389	7577.863
		20312.334	0 5 1	0 4 0	7	2	5	8	2	6	-4.857	7212.158
		20312.398	0 6 1	0 5 0	6	1	6	7	1	7	-4.778	8162.491
		20312.555	0 4 1	0 3 0	11	2	10	12	2	11	-4.344	6517.811
A05	20316.7	20316.699	0 2 1	0 1 0	15	3	12	16	3	13	-5.068	5089.336
A06	20324.3	20324.334	0 3 1	0 1 0	12	3	9	13	11	2	-4.634	5654.780
A07	20331.2	20331.277	0 3 1	0 2 0	13	2	11	14	2	12	-4.937	5786.852
		20331.287	1 3 1	1 2 0	5	1	5	6	1	6	-4.838	7216.297
A08	20334.5	20334.473	0 4 1	0 3 0	11	3	9	12	3	10	-4.410	6767.303
A09	20337.1	20337.375	0 1 2	0 0 1	14	1	14	15	1	15	-4.682	6077.105
A10	20339.8	20339.854	0 2 2	0 1 1	12	1	12	13	1	13	-4.425	7098.995
A11	20342.6	20342.570	0 1 1	0 0 0	18	2	16	19	2	17	-4.828	4331.067
A12	20347.5	20346.986	0 2 2	0 1 1	12	2	11	13	2	12	-4.560	7355.381
		20347.695	0 5 1	0 4 0	9	2	8	10	2	9	-4.301	7542.146
A13	20353.1	20352.932	0 3 1	0 2 0	12	4	8	13	4	9	-4.567	5781.958
		20353.520	0 5 1	0 4 0	9	1	9	10	1	10	-4.266	7254.319
A14	20363.6	20363.252	0 2 1	0 1 0	16	2	14	17	2	15	-4.561	5204.748
		20363.822	1 2 1	1 1 0	8	0	8	9	0	9	-4.904	6134.721
		20363.891	0 5 1	0 4 0	8	1	7	9	1	8	-4.319	7298.575
		20363.895	0 1 1	0 0 0	17	5	12	18	5	13	-5.330	4606.168
A15	20369.5	20369.426	0 4 1	0 3 0	12	1	11	13	1	12	-4.523	6787.653
		20369.828	0 1 3	0 0 2	9	2	8	10	2	9	-4.770	8694.333
A16	20383.3	20383.307	0 3 1	0 2 0	14	1	13	15	1	14	-4.458	5827.338
		20383.332	0 4 1	0 3 0	10	3	7	11	3	8	-4.383	6592.187
A17	20387.3	20387.219	0 2 1	0 1 0	18	9	9	19	9	10	-4.746	7470.305
		20387.338	0 4 1	0 3 0	12	0	12	13	0	13	-4.318	6456.296

* reference number to Fig. 2.
† in Å and in vacuum.
‡ in cm^{-1}.

Table 3. Log $(W/\lambda)_{\rm obs}$* of H_2O Blends in the Region A of 38 M Dwarfs†.

obj.	A01	A02	A03	A04	A05	A06	A07	A08	A09	A10	A11	A12	A13	A14	A15	A16	A17
GJ15A	—	-4.957	-4.803	-4.671	—	-5.018	—	-5.177	—	-5.046	-4.994	—	-5.018	—	—	-4.822	-4.847
GJ105B	-4.757	-4.685	-4.522	-4.405	—	-4.815	-4.711	-4.854	-4.779	-4.739	—	—	-4.772	—	—	-4.587	-4.529
GJ166C	-4.760	-4.709	-4.521	-4.375	—	-4.740	-4.595	-4.772	—	—	—	—	—	—	—	—	-4.430
GJ176	—	-4.981	-4.837	-4.707	—	-5.070	—	-5.233	-5.163	-5.034	—	—	-4.987	—	—	-4.797	-4.793
GJ179	—	-4.837	-4.689	-4.545	—	-4.958	-4.856	-5.061	—	-4.906	—	-4.667	-4.928	-4.673	—	-4.781	-4.674
GJ205	—	-4.986	—	-5.026	—	—	—	—	—	—	—	—	—	—	-5.260	-5.120	-5.173
GJ212	—	-5.052	-5.099	—	—	-5.216	—	-5.272	—	—	—	—	—	-5.060	—	-5.067	-5.035
GJ229	—	-5.032	-5.106	-4.847	—	-5.186	—	-5.297	—	—	—	-4.911	—	—	—	—	-5.098
GJ231.1B	-4.871	-4.796	-4.617	-4.479	—	-4.846	-4.778	-4.924	-4.851	-4.803	-4.670	—	-4.840	-4.544	—	-4.708	-4.636
GJ250B	—	-4.864	-4.802	—	—	-5.073	-4.968	-5.180	-5.070	—	-4.840	-4.778	-4.977	-4.758	—	-4.858	-4.807
GJ273	-4.779	—	-4.562	-4.417	—	-4.787	-4.731	-4.870	-4.767	—	—	-4.537	-4.805	—	—	-4.648	-4.587
GJ324B	-4.834	-4.762	-4.599	-4.475	—	-4.827	-4.861	-4.943	-4.878	-4.836	-4.695	-4.636	-4.870	—	—	-4.694	-4.662
GJ338A	—	—	—	-5.213	—	—	—	—	—	—	—	-5.260	—	—	—	-5.227	-5.227
GJ338B	—	-5.155	—	—	—	-5.590	—	-5.626	—	—	—	-5.304	—	—	—	-5.221	-5.221
GJ406	-4.723	—	-4.438	-4.304	—	-4.693	-4.556	-4.723	-4.636	—	-4.500	—	-4.639	—	—	—	-4.404
GJ411	—	-4.832	-4.681	-4.564	—	-4.996	-4.933	-5.056	-5.020	-4.935	-4.809	-4.691	-4.934	-4.630	—	-4.801	-4.761
GJ412A	—	-4.919	-4.808	-4.666	—	-5.137	—	—	—	-5.112	-4.970	-4.833	-5.065	—	—	-4.893	-4.850
GJ436	-4.963	-4.919	-4.754	-4.618	—	-5.001	-5.008	-5.134	-5.055	-5.005	-4.885	-4.731	-4.978	-4.647	—	-4.822	-4.772
GJ526	—	-4.905	-4.829	-4.696	—	-5.122	-5.131	-5.169	—	-5.064	-4.932	—	-5.030	—	—	-4.875	-4.842
GJ581	-4.918	-4.865	-4.667	-4.506	—	-4.929	—	-5.022	-4.941	—	-4.764	—	-4.873	—	—	-4.721	-4.686
GJ611B	-4.714	—	-4.490	-4.388	-4.936	-4.732	-4.690	-4.852	-4.719	-4.650	—	-4.481	-4.702	—	—	-4.537	-4.466
GJ649	—	-5.041	-5.050	-4.867	—	-5.289	-5.279	-5.402	—	-5.336	-5.219	-5.013	-5.282	—	—	-5.008	-4.989
GJ686	—	-4.851	-4.777	-4.538	—	—	—	—	-5.000	-4.953	-4.828	—	—	-4.759	—	-4.801	—
GJ687	-4.866	—	-4.658	-4.516	—	-4.841	-4.869	-4.909	-4.942	-4.900	-4.747	-4.629	-4.868	-4.586	—	-4.742	-4.696
GJ725A	-4.834	-4.754	-4.599	-4.447	—	-4.837	-4.734	-4.892	-4.860	-4.794	-4.703	—	-4.809	—	—	-4.628	-4.616
GJ725B	-4.810	-4.725	-4.580	-4.411	—	-4.813	-4.706	-4.862	-4.813	-4.743	-4.664	-4.560	-4.801	—	—	-4.590	-4.531
GJ768.1B	—	—	-4.670	-4.520	—	-4.903	-4.870	-4.956	-4.934	-4.909	-4.788	-4.645	-4.874	—	—	-4.732	-4.662
GJ777B	-4.649	—	—	-4.362	—	—	—	—	—	—	—	-4.443	—	—	—	-4.591	-4.446
GJ783.2B	-4.740	—	-4.552	-4.417	—	-4.805	-4.716	-4.884	-4.797	-4.715	-4.625	-4.540	-4.827	—	—	-4.579	-4.500
GJ797B-NE	—	—	-4.681	-4.574	—	-4.984	-4.910	-5.102	-5.043	-4.935	-4.839	-4.686	-4.921	-4.634	—	-4.793	-4.729
GJ797B-SW	—	—	-4.681	-4.578	—	-4.957	-4.902	-5.115	-5.042	-4.918	-4.803	-4.670	-4.906	—	—	-4.761	-4.698
GJ809	—	—	-5.175	-4.950	—	-5.294	—	—	—	-5.449	—	-5.064	—	-4.998	—	-5.102	-5.088
J849	—	-4.908	-4.860	-4.692	—	-5.073	—	-5.092	—	-4.959	-4.867	-4.743	-4.966	—	—	-4.769	-4.757
GJ876	-4.863	—	-4.646	-4.521	—	-4.911	—	-4.972	-4.916	-4.868	-4.732	-4.620	-4.854	—	—	-4.719	-4.712
GJ880	—	-5.015	—	-4.923	—	—	—	—	—	—	—	-4.941	—	-5.116	—	-5.158	-5.138
GJ3348B	—	—	-4.593	-4.456	—	-4.823	-4.817	-4.869	—	—	-4.669	-4.592	-4.804	—	—	-4.660	-4.609
HIP57050	-4.806	—	-4.606	-4.480	—	-4.871	-4.801	-4.955	-4.879	-4.810	-4.683	-4.573	-4.816	—	—	-4.686	-4.608
HIP79431	—	-4.971	-4.914	-4.781	—	-5.168	—	-5.264	—	—	-5.086	-4.904	-5.185	-4.881	—	-4.925	-4.968

* The equivalent widths are measured by referring to the pseudo-continuum.
† The spectroscopic data for the representative line(s) in the H_2O blends through Ref. nos. A01 to A17 are given in Table 2 for the corresponding Ref. nos. Complete listing of this table is available in the online version of the journal.

Table 4. H_2O Lines in the Region B.

Ref.*	λ_{obs}†	λ†	$v_1' v_2' v_3'$	$v_1'' v_2'' v_3''$	J'	K_a'	K_c'	J''	K_a''	K_c''	$\log gf$	L.E.P.‡
B01	22517.5	22517.619	0 2 0	0 0 0	17	8	9	16	5	12	-5.910	3639.538
		22517.760	1 0 0	0 0 0	18	5	14	17	2	15	-5.907	3567.174
B02	22528.7	22528.588	0 1 1	0 1 0	18	8	10	17	6	11	-5.283	5965.714
		22528.871	1 0 0	0 0 0	20	7	14	19	4	15	-5.410	4851.821
B03	22537.6	22537.447	1 0 0	0 0 0	19	6	14	18	3	15	-6.133	4201.253
		22537.570	0 0 1	0 0 0	17	7	11	16	5	12	-5.765	3639.538
B04	22545.3	22545.037	0 1 1	0 1 0	16	6	11	15	4	12	-6.015	4736.242
		22545.221	0 1 1	0 1 0	17	8	9	16	6	10	-5.893	5546.740
		22545.221	0 1 1	0 1 0	14	9	5	13	7	6	-6.016	4643.871
B05	22560.1	22560.082	1 0 0	0 0 0	21	6	15	20	5	16	-5.493	5294.038
B06	22564.2	22564.066	0 0 1	0 0 0	15	9	7	14	7	8	-5.924	3264.337
		22564.504	0 2 1	0 2 0	14	3	11	13	1	12	-5.868	5235.958
B07	22578.9	22579.191	0 0 1	0 0 0	21	8	13	20	6	14	-5.433	5680.788
B08	22585.6	22585.514	0 1 1	0 1 0	15	5	11	14	3	12	-5.741	4184.832
B09	22592.7	22592.391	0 3 0	0 1 0	21	11	10	20	10	11	-5.462	8202.864
		22592.992	2 0 0	0 0 1	21	10	11	20	8	12	-5.055	9615.250
B10	22604.4	22604.469	0 0 1	0 0 0	16	8	9	15	6	10	-6.129	3443.192
B11	22621.4	22621.393	0 1 1	0 1 0	20	7	13	19	5	14	-5.011	6725.862
B12	22623.6	22623.605	0 1 1	0 1 0	14	3	11	13	1	12	-6.054	3654.049
B13	22639.4	22639.680	1 0 0	0 0 0	19	5	14	18	4	15	-5.718	4201.859
B14	22647.4	22647.348	0 0 1	0 0 0	20	8	12	19	6	13	-5.040	5199.596
B15	22649.3	22649.543	0 0 1	0 0 0	15	5	11	14	3	12	-5.910	2551.483
B16	22681.9	22682.061	0 0 1	0 0 0	14	3	11	13	1	12	-6.348	2042.311
B17	22709.1	22709.215	0 0 1	0 0 0	18	8	10	17	6	11	-5.290	4291.907
B18	22724.7	22724.508	0 1 1	0 1 0	15	6	10	14	4	11	-5.585	4396.051
		22724.695	0 0 1	0 0 0	17	8	9	16	6	10	-5.911	3870.201
B19	22740.6	22740.486	0 2 1	0 2 0	13	4	10	12	2	11	-5.895	4967.491
B20	22763.1	22762.836	0 0 1	0 0 0	13	9	4	12	7	5	-6.617	2613.104
		22763.025	0 2 0	0 0 0	27	10	17	26	9	18	-5.205	9368.730
		22763.592	0 3 0	0 1 0	19	11	8	18	10	9	-5.555	7293.308
B21	22768.1	22768.193	0 0 1	0 0 0	12	10	2	11	8	3	-6.765	2522.265
B22	22791.5	22791.547	0 1 1	0 1 0	18	6	12	17	4	13	-5.052	5680.547
B23	22801.6	22801.865	0 0 1	0 0 0	15	6	10	14	4	11	-5.740	2746.023
B24	22839.2	22838.883	0 1 1	0 1 0	13	4	10	12	2	11	-6.056	3386.379
		22839.604	0 2 0	0 0 0	15	8	7	14	5	10	-6.587	2918.245
		22839.834	0 1 1	0 1 0	16	5	11	15	3	12	-5.763	4728.221
B25	22907.9	22907.998	0 1 1	0 1 0	13	3	10	12	1	11	-6.539	3386.052
		22908.092	0 3 0	0 1 0	15	12	3	14	11	4	-6.038	5996.690
B26	22917.9	22918.090	0 0 1	0 0 0	18	7	11	17	5	12	-5.093	4174.288
B27	22931.0	22930.801	0 1 1	0 1 0	16	7	9	15	5	10	-5.317	5015.704
		22931.207	0 2 1	0 2 0	13	5	9	12	3	10	-5.708	5193.882

* reference number to Fig. 3.
† in Å and in vacuum.
‡ in cm^{-1}.

Table 5. Log $(W/\lambda)_{\rm obs}$* of H_2O Blends in the Region B of 20 M Dwarfs†.

obj.	B01	B02	B03	B04	B05	B06	B07	B08	B09	B10	B11	B12	B13	B14	B15	B16	B17	B18	B19	B20	B21	B22	B23	B24	B25	B26	B27
GJ105B	-5.229	-5.078	-5.268	—	—	-5.476	—	—	—	—	-5.262	—	-5.152	-5.128	—	-5.451	-5.245	-5.322	—	—	—	-5.059	—	—	—	-5.049	-5.097
GJ166C	-5.191	-5.060	-5.351	—	—	—	-4.884	—	-5.172	-5.216	-5.274	—	-5.140	-5.133	—	-5.244	-5.081	-5.138	—	-4.981	—	-5.105	—	-4.910	-5.322	-5.017	-5.038
GJ179	-5.439	-5.321	-5.470	-5.430	—	-5.592	-5.194	—	—	—	-5.416	—	-5.522	-5.429	—	-5.518	-5.186	-5.612	—	—	—	—	-5.376	-5.087	—	-5.111	-5.218
GJ231.1B	-5.421	-5.307	-5.432	-5.322	—	—	-5.189	—	-5.433	—	-5.290	—	—	-5.102	—	-5.432	-5.302	-5.495	—	—	—	—	—	-5.365	-5.563	-5.212	-5.367
GJ273	-5.526	-5.249	-5.320	-5.259	—	—	-5.023	—	-5.256	—	-5.320	—	—	-5.269	-5.341	—	-5.209	-5.437	—	-5.239	-5.412	-5.452	—	—	-5.363	-5.151	-5.190
GJ324B	—	-5.297	-5.269	-5.399	—	-5.555	-5.207	—	-5.505	—	—	—	-5.328	-5.548	—	-5.539	-5.226	-5.555	—	-5.306	—	-5.593	-5.446	—	-5.670	-5.267	-5.345
GJ406	-5.091	-4.973	-5.210	-5.071	—	-5.212	—	-5.106	-5.158	-5.286	-5.317	-5.465	-5.103	-5.050	—	-5.273	-5.022	-5.186	—	—	-5.222	-5.179	—	-4.857	-5.185	-4.859	—
GJ581	—	-5.304	—	-5.404	—	—	-5.157	—	—	—	—	—	—	-5.383	—	-5.569	-5.338	-5.420	—	—	—	—	—	-5.174	—	-5.046	-5.279
GJ611B	-4.918	-5.064	-5.255	-5.267	-5.217	-5.398	-4.893	—	-5.184	-5.147	-5.269	—	-5.232	-5.169	—	-5.564	-5.232	-5.224	—	-5.274	—	-5.187	—	-5.002	-5.348	-5.028	-5.157
GJ687	—	-5.249	—	—	—	—	—	—	—	—	-5.445	—	-5.253	-5.356	-5.547	—	-5.424	-5.558	—	—	-5.439	-5.388	-5.382	—	—	-5.244	-5.405
GJ725A	-5.323	-5.227	-5.386	-5.306	-5.380	-5.600	-5.041	—	-5.400	—	-5.269	—	-5.255	-5.383	—	-5.405	-5.310	-5.328	—	—	-5.577	-5.494	—	-5.224	—	-5.115	-5.187
GJ725B	-5.117	-5.096	—	-5.246	-5.374	-5.588	-5.011	-5.371	-5.295	-5.349	-5.261	—	-5.189	-5.401	—	-5.404	-5.248	-5.382	-5.279	—	-5.682	-5.418	-5.287	-5.163	—	-5.088	-5.120
GJ768.1B	—	-5.262	—	-5.183	—	—	-4.999	—	—	—	—	—	-5.204	-5.346	—	-5.531	-5.381	—	—	—	—	-5.492	—	-5.222	-5.424	-5.203	—
GJ777B	-5.106	-5.128	-5.321	-5.183	-5.130	-5.350	—	—	-5.274	-5.179	-5.386	—	-5.156	-5.188	—	-5.551	-5.134	-5.234	-5.188	—	—	-5.219	—	—	—	-5.058	-5.106
GJ783.2B	-5.163	-5.133	-5.421	-5.287	-5.275	-5.507	-4.964	-5.294	-5.253	—	-5.326	—	-5.219	-5.204	-5.393	-5.463	-5.226	-5.306	-5.223	—	—	-5.351	—	-5.050	-5.530	-5.053	-5.115
GJ797B-NE	—	-5.344	—	—	—	—	—	—	—	—	—	—	-5.375	-5.407	-5.523	—	-5.587	—	—	-5.540	—	-5.659	—	—	—	—	-5.456
GJ797B-SW	—	-5.345	—	—	—	—	—	—	—	—	—	—	-5.385	-5.434	-5.548	—	—	—	—	-5.506	—	-5.570	—	—	—	—	-5.410
GJ876	—	-5.243	—	-5.350	—	—	—	—	-5.507	—	—	—	—	-5.204	—	—	-5.286	-5.487	—	—	—	—	—	—	—	—	-5.225
GJ3348B	-5.350	-5.153	—	-5.161	—	-5.368	—	—	-5.254	—	—	—	-5.287	—	—	-5.506	-5.348	-5.553	—	-5.167	—	-5.274	—	—	—	-4.932	—
HIP57050	-5.290	-5.210	—	-5.311	-5.277	-5.605	-5.115	—	-5.426	—	-5.389	—	-5.288	-5.248	—	-5.455	-5.362	-5.263	-5.422	-5.250	—	-5.477	—	-5.159	—	-5.077	-5.232

* The equivalent widths are measured by referring to the pseudo-continuum.
† The spectroscopic data for the representative line(s) in the H_2O blends through Ref. nos. B01 to B27 are given in Table 4 for the corresponding Ref. nos. Complete listing of this table is available in the online version of the journal.

Table 6. Oxygen Abundances ($\log A_{\rm O}^{A}$) from the H_2O Lines in the Region A.

obj.	$\log A_{\rm C}$*	$\Delta\log A_{\rm O}^{A}$†	$\log A_{\rm O}^{A} \pm$ p.e.	N_A‡	χ^2_-§	χ^2_0‖	χ^2_+#
GJ 15A	-3.601	-0.012	-3.313 ± 0.013	10	3.947	2.644	3.987
GJ 105B	-3.468	+0.026	-3.142 ± 0.033	12	7.605	7.554	9.413
GJ 166C	-3.366	+0.039	-3.027 ± 0.043	8	14.971	12.498	11.775
GJ 176	-3.352	-0.101	-3.153 ± 0.021	10	8.747	4.841	7.720
GJ 179	-3.427	-0.074	-3.201 ± 0.021	12	7.146	4.549	6.724
GJ 205	-3.116	-0.152	-2.968 ± 0.046	5	2.519	4.037	9.772
GJ 212	-3.296	-0.101	-3.097 ± 0.027	7	2.553	2.134	4.696
GJ 229	-3.271	-0.133	-3.104 ± 0.022	7	1.969	2.122	6.164
GJ 231.1B	-3.572	+0.037	-3.235 ± 0.035	14	4.839	5.106	7.874
GJ 250B	-3.413	-0.078	-3.191 ± 0.031	12	3.962	2.618	4.624
GJ 273	-3.403	-0.015	-3.118 ± 0.023	11	15.290	12.533	14.772
GJ 324B	-3.360	-0.103	-3.163 ± 0.041	14	9.319	6.069	9.544
GJ 338A	-3.587	-0.030	-3.317 ± 0.026	4	1.757	1.700	2.668
GJ 338B	-3.578	-0.034	-3.312 ± 0.058	6	1.542	2.167	4.166
GJ 406	-3.612	-0.088	-3.400 ± 0.023	10	10.510	13.204	22.045
GJ 411	-3.671	-0.001	-3.372 ± 0.030	14	7.784	5.624	8.727
GJ 412A	-3.849	+0.019	-3.530 ± 0.029	10	6.765	4.423	7.272
GJ 436	-3.634	-0.082	-3.416 ± 0.018	15	7.506	3.676	7.794
GJ 526	-3.553	-0.025	-3.278 ± 0.026	11	6.650	4.851	9.105
GJ 581	-3.560	-0.015	-3.275 ± 0.021	11	9.629	7.148	10.703
GJ 611B	-3.762	+0.137	-3.325 ± 0.053	13	11.089	10.892	12.478
GJ 649	-3.544	-0.094	-3.338 ± 0.026	12	2.819	1.304	3.019
GJ 686	-3.497	-0.033	-3.230 ± 0.030	8	3.416	3.157	5.112
GJ 687	-3.428	-0.090	-3.218 ± 0.030	14	13.681	8.685	14.452
GJ 725A	-3.584	+0.035	-3.249 ± 0.037	13	5.835	6.069	8.940
GJ 725B	-3.605	+0.046	-3.259 ± 0.053	14	9.752	9.755	12.871
GJ 768.1C	-3.504	-0.028	-3.232 ± 0.022	12	1.789	1.278	1.913
GJ 777B	-3.239	-0.045	-2.984 ± 0.078	5	2.560	2.104	2.164
GJ 783.2B	-3.413	-0.003	-3.116 ± 0.051	13	12.113	10.850	13.617
GJ 797B-NE	-3.535	-0.053	-3.288 ± 0.021	13	2.152	1.265	1.954
GJ 797B-SW	-3.506	-0.057	-3.263 ± 0.024	12	2.127	1.255	1.999
GJ 809	-3.550	-0.118	-3.368 ± 0.031	8	3.943	1.809	2.146
GJ 849	-3.270	-0.116	-3.086 ± 0.016	11	8.274	5.173	11.741
GJ 876	-3.355	-0.089	-3.144 ± 0.030	12	5.098	3.155	5.331
GJ 880	-3.348	-0.133	-3.181 ± 0.034	6	2.890	1.897	5.065
GJ 3348B	-3.400	-0.004	-3.104 ± 0.030	10	1.309	1.097	1.460
HIP 57050	-3.259	-0.093	-3.052 ± 0.038	13	13.003	8.453	13.002
HIP 79431	-3.236	-0.175	-3.111 ± 0.014	11	8.007	3.314	13.338

* from Paper I.

† The correction to be applied to the initial assumed value of $\log A_{\rm O}^{0} = \log A_{\rm C} + 0.30$.

‡ Number of H_2O blends used in the analysis (see Table 3 as for the Ref. Nos. and EWs of the blends used).

§ χ^2 value for the fitting of the predicted spectrum with $\log A_{\rm O}^{A}$ - 0.05 and the observed one.

‖ χ^2 value for the fitting of the predicted spectrum with $\log A_{\rm O}^{A}$ in the fourth column and the observed one (see Fig. 7).

\# χ^2 value for the fitting of the predicted spectrum with $\log A_{\rm O}^{A}$ + 0.05 and the observed one.

Table 7. Oxygen Abundances ($\log A_{\rm O}^{B}$) from the H_2O Lines in the Region B.

obj.	$\Delta\log A_{\rm O}^{A*}$	$\log A_{\rm O}^{A} \pm$ p.e.*	$\Delta\log A_{\rm O}^{B\dagger}$	$\log A_{\rm O}^{B} \pm$ p.e.	$N_B^{\ddagger}$	diff[§]
GJ 105B	+0.026	-3.142 ± 0.033	+0.040	-3.128 ± 0.050	13	+0.014
GJ 166C	+0.039	-3.027 ± 0.043	+0.033	-3.033 ± 0.074	18	-0.006
GJ 179	-0.074	-3.201 ± 0.021	-0.044	-3.171 ± 0.062	16	+0.030
GJ 231.1B	+0.037	-3.235 ± 0.035	+0.028	-3.244 ± 0.064	15	-0.009
GJ 273	-0.015	-3.118 ± 0.023	-0.034	-3.137 ± 0.047	17	-0.019
GJ 324B	-0.103	-3.163 ± 0.041	-0.112	-3.172 ± 0.040	17	-0.009
GJ 406	-0.088	-3.400 ± 0.023	-0.086	-3.398 ± 0.032	20	+0.002
GJ 581	-0.015	-3.275 ± 0.021	+0.024	-3.236 ± 0.047	10	+0.039
GJ 611B	+0.137	-3.325 ± 0.053	+0.087	-3.375 ± 0.058	21	-0.050
GJ 687	-0.090	-3.218 ± 0.030	-0.093	-3.221 ± 0.034	12	-0.003
GJ 725A	+0.035	-3.249 ± 0.037	+0.004	-3.280 ± 0.050	19	-0.031
GJ 725B	+0.046	-3.259 ± 0.053	-0.001	-3.306 ± 0.062	22	-0.047
GJ 768.1C	-0.028	-3.232 ± 0.022	+0.037	-3.167 ± 0.056	11	+0.065
GJ 777B	-0.045	-2.984 ± 0.078	-0.092	-3.031 ± 0.037	18	-0.047
GJ 783.2B	-0.003	-3.116 ± 0.051	-0.035	-3.148 ± 0.051	22	-0.032
GJ 797B-NE	-0.053	-3.288 ± 0.021	-0.034	-3.269 ± 0.049	8	+0.019
GJ 797B-SW	-0.057	-3.263 ± 0.024	-0.045	-3.251 ± 0.036	7	+0.012
GJ 876	-0.089	-3.144 ± 0.030	-0.065	-3.120 ± 0.056	7	+0.024
GJ 3348B	-0.004	-3.104 ± 0.030	+0.041	-3.059 ± 0.063	12	+0.045
HIP 57050	-0.093	-3.052 ± 0.038	-0.084	-3.043 ± 0.047	19	+0.009

* results from H_2O Lines in the region A (see Table 6).
† The correction to be applied to the initial assumed value of $\log A_{\rm O}^{0} = \log A_{\rm C}$ +0.30 ($\log A_{\rm C}$ is from Paper I and reproduced in the second column of Table 6).
‡ Number of H_2O blends used in the analysis (see Table 5 as for the Ref. Nos. and EWs of the blends used).
§ diff = $\log A_{\rm O}^{B}$ - $\log A_{\rm O}^{A}$.

Table 8. Carbon and Oxygen Abundances in M Dwarfs.

obj.	$\log A_{\rm C} \pm$ p.e.*	$\log A_{\rm O} \pm$ p.e.†	$\log A_{\rm O}/A_{\rm C}$
GJ 15A	-3.60 ± 0.11	-3.31 ± 0.01A	0.29
GJ 105B	-3.47 ± 0.06	-3.14 ± 0.04	0.33
GJ 166C	-3.37 ± 0.14	-3.03 ± 0.06	0.34
GJ 176‡	-3.35 ± 0.07	-3.15 ± 0.02A	0.20
GJ 179‡	-3.43 ± 0.11	-3.18 ± 0.04	0.24
GJ 205	-3.12 ± 0.08	-2.97 ± 0.05A	0.15
GJ 212	-3.30 ± 0.11	-3.10 ± 0.03A	0.20
GJ 229	-3.27 ± 0.07	-3.10 ± 0.02A	0.17
GJ 231.1B	-3.57 ± 0.05	-3.24 ± 0.05	0.33
GJ 250B	-3.41 ± 0.10	-3.19 ± 0.03A	0.22
GJ 273	-3.40 ± 0.11	-3.13 ± 0.04	0.27
GJ 324B	-3.36 ± 0.13	-3.17 ± 0.04	0.19
GJ 338A	-3.59 ± 0.04	-3.32 ± 0.03A	0.27
GJ 338B	-3.58 ± 0.04	-3.31 ± 0.06A	0.27
GJ 406	-3.61 ± 0.10	-3.40 ± 0.03	0.21
GJ 411	-3.67 ± 0.06	-3.37 ± 0.03A	0.30
GJ 412A	-3.85 ± 0.04	-3.53 ± 0.03A	0.32
GJ 436‡	-3.63 ± 0.06	-3.42 ± 0.02A	0.22
GJ 526	-3.55 ± 0.04	-3.28 ± 0.03A	0.27
GJ 581‡	-3.56 ± 0.05	-3.26 ± 0.03	0.30
GJ 611B	-3.76 ± 0.03	-3.36 ± 0.06	0.41
GJ 649‡	-3.54 ± 0.04	-3.34 ± 0.03A	0.21
GJ 686	-3.50 ± 0.04	-3.23 ± 0.03A	0.27
GJ 687	-3.43 ± 0.09	-3.22 ± 0.03	0.21
GJ 725A	-3.58 ± 0.09	-3.27 ± 0.05	0.32
GJ 725B	-3.61 ± 0.08	-3.29 ± 0.06	0.32
GJ 768.1C	-3.50 ± 0.08	-3.20 ± 0.04	0.30
GJ 777B	-3.24 ± 0.16	-3.02 ± 0.05	0.22
GJ 783.2B	-3.41 ± 0.10	-3.14 ± 0.05	0.28
GJ 797B-NE	-3.54 ± 0.09	-3.28 ± 0.03	0.25
GJ 797B-SW	-3.51 ± 0.09	-3.26 ± 0.03	0.25
GJ 809	-3.55 ± 0.04	-3.37 ± 0.03A	0.18
GJ 849‡	-3.27 ± 0.09	-3.09 ± 0.02A	0.18
GJ 876‡	-3.36 ± 0.13	-3.14 ± 0.04	0.22
GJ 880	-3.35 ± 0.07	-3.18 ± 0.03A	0.17
GJ 3348B	-3.40 ± 0.11	-3.08 ± 0.05	0.32
HIP 57050‡	-3.26 ± 0.12	-3.05 ± 0.04	0.21
HIP 79431‡	-3.24 ± 0.12	-3.11 ± 0.01A	0.12
the Sun1§	-3.44 ± 0.04	-3.07 ± 0.035	0.37
the Sun2‖	-3.57 ± 0.05	-3.31 ± 0.05	0.26

* from Paper I.
† For the case with A attached, the same as $\log A_{\rm O}^{A}$ in Tables 6. Otherwise, the weighted mean of $\log A_{\rm O}^{A}$ and $\log A_{\rm O}^{B}$ from Tables 6 and 7, respectively.
‡ Planet hosting M dwarf.
§ Anders & Grevesse (1989).
‖ Asplund et al. (2009).

Table 9. O/Fe Ratios in M Dwarfs.

obj.	[Fe/H]*	$\log A_{\rm Fe}$	$\log A_{\rm O}$†	$\log A_{\rm O}/A_{\rm Fe}$
GJ 15A	-0.35‡	-4.85	-3.31	1.54
GJ 205	+0.6§	-3.90	-2.97	0.93
GJ 229	+0.2‡	-4.30	-3.10	1.20
GJ 411	-0.2§	-4.70	-3.37	1.33
GJ 105B	-0.06‖	-4.56	-3.14	1.42
GJ 176	+0.04‖	-4.46	-3.15	1.31
GJ 250B	-0.05‖	-4.55	-3.19	1.36
GJ 436	+0.08‖	-4.42	-3.42	1.00
GJ 581	-0.15‖	-4.65	-3.26	1.39
GJ 849	+0.35‖	-4.15	-3.09	1.06
GJ 876	+0.12‖	-4.38	-3.14	1.24
GJ 105B	-0.02#	-4.52	-3.14	1.38
GJ 166C	+0.08#	-4.42	-3.03	1.39
GJ 176	-0.01#	-4.51	-3.15	1.36
GJ 205	+0.22#	-4.28	-2.97	1.31
GJ 229	-0.01#	-4.51	-3.10	1.41
GJ 250B	-0.10#	-4.60	-3.19	1.41
GJ 273	-0.01#	-4.51	-3.13	1.38
GJ 406	+0.18#	-4.32	-3.40	0.92
GJ 526	-0.20#	-4.70	-3.28	1.42
GJ 581	-0.21#	-4.71	-3.26	1.45
GJ 686	-0.37#	-4.87	-3.23	1.64
GJ 849	+0.24#	-4.26	-3.09	1.17
GJ 876	+0.15#	-4.35	-3.14	1.21
GJ 880	+0.07#	-4.43	-3.18	1.25
the Sun1	0.00	-4.50**	-3.07***	1.43
the Sun2	0.00	-4.50**	-3.31**	1.19

* [Fe/H] = $\log A_{\rm Fe}^{*}$ - $\log A_{\rm Fe}^{\odot}$.
† from Table 8.
‡ Mould (1978)
§ [M/H] (Mould 1978) is used for [Fe/H].
‖ [M/H] (Önehag et al. 2012) based on several metals including Fe.
Neves et al. (2013)
** Asplund et al. (2009)
*** Anders & Grevesse (1989)

Table 10. Fundamental Parameters Based on $T_{\rm eff}$ by the Interferometry.

obj.	sp.ty.*	p(msec)†	$F_{3.4}$(mag)‡	$M_{3.4}$(mag)§	$F_{3.4}$(mag)‖	$M_{3.4}$(mag)§	$T_{\rm eff}$
GJ 15A	dM2.5	278.76 ± 0.77	3.853 ± 0.099	6.08 ± 0.10	3.872 ± 0.381	6.10 ± 0.39	3563 ± 11
GJ 53A	G5Vp	132.38 ± 0.82	3.326 ± 0.141	3.94 ± 0.15	3.311 ± 0.487	3.92 ± 0.50	5348 ± 26
GJ 75	K0V	99.33 ± 0.53	3.753± 0.091	3.74 ± 0.10	3.725 ± 0.278	3.71 ± 0.29	5398 ± 75
GJ 176#	dM2.5e	107.83 ± 2.85	5.434 ± 0.066	5.60 ± 0.12	5.486 ± 0.177	5.65 ± 0.23	3679 ± 77
GJ 205	dM3	176.77 ± 1.18	3.743 ± 0.120	4.98 ± 0.13	3.790 ± 0.519	5.03 ± 0.53	3801 ± 9
GJ 412A	dM2	206.27 ± 1.00	4.638 ± 0.085	6.21 ± 0.10	4.641 ± 0.312	6.21 ± 0.32	3497 ± 39
GJ 436	dM3.5	98.61 ± 2.33	5.987 ± 0.052	5.96 ± 0.10	6.017 ± 0.110	5.99 ± 0.16	3416 ± 53
GJ 526	dM3	185.49 ± 1.10	4.372 ± 0.095	5.71 ± 0.11	4.191 ± 0.426	5.53 ± 0.44	3618 ± 31
GJ 551	M5.5V	771.64 ± 2.60	4.195 ± 0.086	8.63 ± 0.09	4.207 ± 0.331	8.64 ± 0.34	3054 ± 79
GJ 570A	K4V	171.22 ± 0.94	3.159 ± 0.012	4.33 ± 0.02	3.474 ± 0.387	4.64 ± 0.40	4507 ± 58
GJ 581	dM4	160.91 ± 2.62	5.694 ± 0.055	6.73 ± 0.09	5.743 ± 0.094	6.78 ± 0.13	3442 ± 54
GJ 631	K0V	102.55 ± 0.40	3.797 ± 0.110	3.85 ± 0.12	3.882 ± 0.325	3.94 ± 0.33	5337 ± 41
GJ 649#	dM2	96.67 ± 1.39	5.502 ± 0.065	5.43 ± 0.10	5.559 ± 0.139	5.49 ± 0.17	3690 ± 45
GJ 687	dM4	220.84 ± 0.94	4.397 ± 0.094	6.12 ± 0.10	4.398 ± 0.268	6.12 ± 0.28	3413 ± 28
GJ 725A	dM4	280.18 ± 2.18	4.498 ± 0.226	6.74 ± 0.24	4.065 ± 0.494	6.30 ± 0.51	3407 ± 15
GJ 809	dM2	141.87 ± 0.64	4.501 ± 0.088	5.26 ± 0.10	4.518 ± 0.272	5.28 ± 0.28	3692 ± 22
GJ 876#	dM4.5	213.28 ± 2.12	4.844 ± 0.077	6.49 ± 0.10	4.863 ± 0.243	6.51 ± 0.26	3129 ± 19
GJ 880	dM2.5	146.09 ± 1.00	4.432 ± 0.080	5.26 ± 0.09	4.396 ± 0.353	5.22 ± 0.37	3713 ± 11

* The spectral types for M dwarfs we analyze in this paper are by Joy & Abt (1974) and those for other objects from Boyajian et al. (2012).
† Parallax by Hipparcos (van Leeuwen 2007).
‡ $W1$ band flux centered at 3.4 μm from the WISE All-Sky Release (Wright et al. 2010).
§ Absolute magnitude at 3.4 μm based on the $F_{3.4}$ in the preceding column.
‖ $W1$ band flux centered at 3.4 μm from the AllWISE Catalogue (Wright et al. 2010).
Based on new angular diameter measurements by von Braun et al. (2014), which has been published after Paper I.

Table 11. Fundamental Parameters Based on $T_{\rm eff}$ by the Infrared Flux Method.

obj.	sp.ty.*	p(msec)†	$F_{3.4}$(mag)‡	$M_{3.4}$(mag)§	$F_{3.4}$(mag)‖	$M_{3.4}$(mag)§	$T_{\rm eff}$#
GJ 273-L**	dM4	262.98 ± 1.39	4.723 ± 0.074	6.82 ± 0.09	4.787 ± 0.223	6.89 ± 0.23	3150 ± 95
GJ 406	dM6.5e	419.10 ± 2.10	5.807 ± 0.055	8.92 ± 0.07	5.836 ± 0.138	8.95 ± 0.15	2800 ± 85
GJ 644C	M7V	148.92 ± 4.00	8.588 ± 0.023	9.45 ± 0.08	8.619 ± 0.023	9.48 ± 0.08	2640 ± 80
GJ 752A	M3V	170.36 ± 1.00	4.466 ± 0.078	5.62 ± 0.09	4.379 ± 0.262	5.54 ± 0.27	3475± 105
GJ 752B	M8V	170.36 ± 1.00	8.465 ± 0.023	9.62 ± 0.04	8.317 ± 0.023	9.47 ± 0.04	2250 ± 70
GJ 884	dM0.5	121.69 ± 0.69	4.424 ± 0.087	4.85 ± 0.10	4.324 ± 0.273	4.75 ± 0.29	3850 ± 115
GJ 3849	M9V	95.00 ± 5.70	10.431 ± 0.023	10.32 ± 0.15	10.428 ± 0.022	10.32 ± 0.15	2130 ± 65

* The spectral types for M dwarfs we analyze in this paper are by Joy & Abt (1974) and those for other objects from Tsuji et al. (1996).
† Parallax by Hipparcos (van Leeuwen 2007), except for GJ 406 and GJ 644C by RECONS and GJ 3849 by Gliese & Jahreiss (1991).
‡ $W1$ band flux centered at 3.4 μm from the WISE All-Sky Release (Wright et al. 2010).
§ Absolute magnitude at 3.4 μm based on the $F_{3.4}$ in the preceding column.
‖ $W1$ band flux centered at 3.4 μm from the AllWISE Catalog(Wright et al. 2010).
Errors estimated from those of the photometric data.
** We apply different $T_{\rm eff}$ values - low and high - for this object, and L implies that this is the case of low $T_{\rm eff}$ (see subsection 3.1).